IEEE Access
Multidisciplinary | Rapid Review | Open Access Journal

Received March 8, 2022, accepted April 10, 2022, date of publication April 18, 2022, date of current version April 26, 2022.

Digital Object Identifier 10.1109/ACCESS.2022.3168353

Magnetically Decoupled Modular Coil Array for Dynamic Wireless Power Transfer With Magnetic Beamforming

KYUNGTAE KIM[1], HAN-JOON KIM[2], (Member, IEEE), DONG-WOOK SEO[3], (Senior Member, IEEE), AND JI-WOONG CHOI[1], (Senior Member, IEEE)

[1]Department of Electrical Engineering and Computer Science, Daegu Gyeongbuk Institute of Science and Technology (DGIST), Daegu 42988, Republic of Korea
[2]Department of Electrical Engineering, National University of Singapore (NUS), Singapore 80523
[3]Department of Electronic and Electrical Information Engineering, Korea Maritime and Ocean University (KMOU), Busan 80309, Republic of Korea

Corresponding authors: Han-Joon Kim (elekhj@nus.edu.sg) and Ji-Woong Choi (jwchoi@dgist.ac.kr)

This work was supported in part by the Ministry of Science and ICT (MSIT) of the Korean Government through the Bio and Medical Technology Development Program of the National Research Foundation (NRF) under Grant NRF-2017M3A9G8084463, in part by the MSIT of the Korean Government through NRF under Grant NRF-2021R1A2C2008415, and in part by the MSIT of the Korean Government through Daegu Gyeongbuk Institute of Science and Technology (DGIST) Research and Development Program under Grant DGIST-22-CoE-IT-01.

ABSTRACT Dynamic wireless power transfer (DWPT) has emerged as a technology for delivering sustainable energy to mobile electric vehicles without charging cables. Magnetic beamforming is a well-known DWPT strategy for increasing power transfer efficiency (PTE) by calculating an optimal weight for focusing the magnetic fields from the transmitting (TX) coils to the desired receiving (RX) coils. However, when magnetic beamforming is applied to multi-inputs and multi-outputs (MIMO) WPT, the cross-coupling at TX and RX coils inevitably emerges, resulting in deterioration of the PTE and power factor (PF). This paper presents a magnetically decoupled modular coil array for MIMO-WPT applicable to a DWPT environment. First, we present a mathematical analysis of the influences of magnetic couplings in MIMO-WPT. Then, we derive the criteria of magnetic couplings in terms of improved PTE and PF and design a modular coil array that satisfies the derived criteria. Finally, we compare the proposed modular coil array with an existing square coil array in a DWPT environment via a 3D finite element analysis simulator. The proposed modular coil array achieves PTE improvement of up to 30 %, whereas the existing square coil array ends up to 18 %, as the number of receiving coils increases from one to five. In addition, the PF of the proposed modular coil array is close to 1.0, whereas that of the existing square coil array is attenuated up to 0.5.

INDEX TERMS Magnetic beamforming, cross-coupling, dynamic wireless power transfer (DWPT), modular coil array, 3D finite element analysis (FEM), power transfer efficiency, power factor.

I. INTRODUCTION

Various industries, such as those that make mobile devices, sensors, vehicles, and biomedical devices, have shown interest in wireless power transfer (WPT) [1]–[3]. The best-known WPT technique is resonant inductive power transfer (RIPT), which uses a magnetic field as a power transmission medium [4]. As shown in Fig. 1, a WPT system using the RIPT technique is configured as a power source, compensation network, rectifier, load, and magnetic coupler composed of transmitting (TX) and receiving (RX) coils. However, the RIPT technique has a limited charging distance due to the rapid decay of the magnetic field. Despite this drawback, it has been widely utilized owing to its simple structure, the convenience of use, and safety.

As an application of the RIPT technique, dynamic wireless power transfer (DWPT) for charging a moving receiver has recently been in the spotlight in vehicle industries, such as for electric/hybrid vehicles [1], unmanned aerial vehicles [5], and automatic guided vehicles [6]. There are two structures of magnetic couplers available for DWPT: lumped and distributed topologies [7], [8]. The lumped topology utilizes a long track coil laid beneath the road. It achieves a low cost advantage, but high power transfer efficiency (PTE) is

The associate editor coordinating the review of this manuscript and approving it for publication was F. R. Islam.

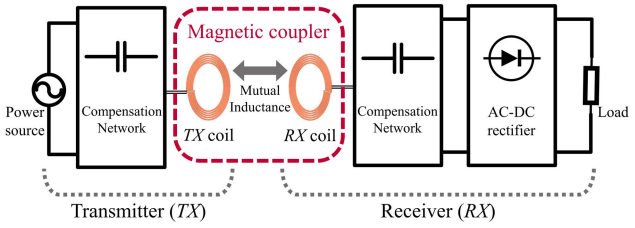

FIGURE 1. Structure of WPT using RIPT technique.

challenging to achieve because of the low quality factor and coupling. The distributed topology involves an arrangement of multiple small coils and shows relatively better performance than the lumped topology.

However, the distributed topology requires a complicated control algorithm to switch the output power of the TX coils based on the position of a moving object. Despite the control system, the received power in the distributed topology may be reduced or even zero when the moving object passes between the TX coils [9]. This phenomenon where the received power repeatedly increases and decreases is called the power pulsation problem, and it occurs because the magnetic field strength varies depending on the object's position. This power pulsation problem is typically solved by rearranging the TX coils to minimize any gaps between them [10].

Meanwhile, magnetic beamforming is a promising technology that can overcome the power pulsation problem and increase the average performance of the WPT system [11]. With this technology, the magnetic fields from the TX coils are focused at the location where the RX coils are located by adjusting the TX voltages and currents, which transfers more power to the devices. In [11], magnetic beamforming is applied for the first time to a multi-inputs and single-output (MISO)-WPT having multiple TX coils and a single RX coil. The same research team extended the work done in [11] to include multi-inputs and multi-outputs (MIMO)-WPT having numerous TX coils and RX coils in [12].

However, it is necessary to arrange several TX coils to apply magnetic beamforming, which causes cross-coupling between TX coils. Typically, the cross-coupling causes performance degradation such as field leakage [13], phase distortion [14], and power attenuation [10]. In [15], the influences of cross-coupling between TX coils in MISO-WPT with magnetic beamforming was analyzed, and it was verified that cross-coupling causes power factor (PF) attenuation. However, this study only considered the arrangement of a single RX coil. Therefore, the first contribution here is to do a theoretical analysis of the influences of all magnetic coupling of MIMO-WPT with magnetic beamforming and then derive the criteria for improving PTE and PF.

According to [16], a design of a magnetic coupler (TX and RX array) is critical for good WPT performance; therefore, the second contribution here is to design a magnetic coupler satisfying the derived criteria. As will be explained in the text, the fewer cross-couplings between the TX and RX coils, the better the WPT performance in PTE and PF. There are many studies regarding the reduction of the cross-coupling between coils [17]–[24]. These studies, however, may not be suitable for use in magnetic beamforming for the following reasons: coil shape [17]–[19], variation of self-inductance [20], different direction of magnetic flux [21], limited number of coils [22], [23], and requirement for additional power [24].

Therefore, we proposed a modular coil array with the reduced cross-couplings between coils in the same array and the increased magnetic couplings when used to form TX and RX arrays for MIMO-WPT. Our proposed modular coil array is based on a modified-bipolar coil with a bent structure to facilitate assembly to provide a flat surface when forming an array. Under the DWPT environment modeled using 3D finite element method (FEM) simulation, the modular coil array outperforms the existing square coil array in PTE and PF.

In summary, the contributions of this paper are:

- **Analysis** of the influences of all magnetic couplings in MIMO-WPT with magnetic beamforming.
- **Derivation** of the criteria for magnetic couplings in terms of improved PTE and PF.
- **Proposal** of a modular coil array satisfying the derived criteria.
- **Demonstration** of the superior performance of the proposed modular coil array than the existing square coil array in a DWPT environment.

This paper is organized as follows. Section II provides a theoretical background. Section III is a theoretical analysis of the magnetic couplings of MIMO-WPT and derives relationships between these couplings and the PTE and PF. Section IV proposes a modular coil array suitable for MIMO-WPT with magnetic beamforming. Section V provides a performance comparison between the existing square coil array and the proposed modular coil array in a DWPT environment via 3D FEM simulation. Finally, Section VI offers the conclusion.

II. THEORETICAL BACKGROUND

A. CIRCUIT MODELING FOR WPT

The WPT using the RIPT technique in Fig. 1 can be described using circuit equations as follows [12].

1) SISO-WPT

Fig. 2 shows a schematic of a SISO-WPT: (a) a typical circuit and (b) an equivalent circuit of TX and RX at resonant state. C, L, and R denote the capacitance, self-inductance, and the intrinsic resistance of the coil, respectively. V and I denote the voltage source and current, respectively. The subscripts T and R denote the TX and RX. The terms TX and RX refer to transmitting and receiving when used with other nouns, while they refer to transmitter and receiver when used alone. R_L denotes the load impedance indicating the charging device. M denotes a mutual inductance calculated by $M = k\sqrt{L_T L_R}$, where k is a coupling coefficient determined by the distance and orientation of both coils L_T and L_R.

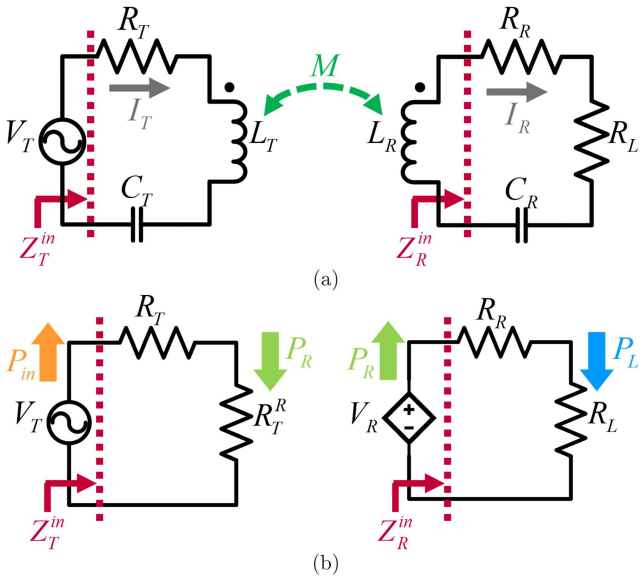

FIGURE 2. Schematic of SISO-WPT: (a) typical circuit and (b) equivalent circuit at resonant state.

We use a series-series (S-S) compensation network to bring the TX and RX circuits into a resonant state at the same frequency. The S-S topology is commonly utilized in the automotive industry due to its advantages as a simple topology with an independent load [25]. The inductance L and capacitance C of the S-S topology are chosen to cancel each other at the resonant frequency ω_r (*i.e.*, $j\omega_r L + 1/j\omega_r C = 0$). Fig. 2(b) is an equivalent circuit at ω_r, and the TX and RX circuits are described by the following two equations:

$$V_R = Z_R^{in} I_R = j\omega_r M I_T, \tag{1}$$

$$V_T = Z_T^{in} I_T = \left(R_T + R_T^R\right) I_T, \tag{2}$$

where R_T^R is the reflected resistance appearing at TX from RX and it is calculated by $R_T^R = {\omega_r}^2 M^2 / Z_R^{in}$. Z_T^{in} and Z_R^{in} are the input impedance seen from V_T and V_R, respectively.

Equation (1) describes how the TX current I_T induces RX voltage and current, V_R and I_R. The influence from the TX to RX appears as a current-dependent voltage source V_R, as shown in Fig. 2(b). Equation (2) describes the RX influence on the TX as a reflected resistance R_T^R. Based on (1), (2), and Fig. 2(b), the PTE, denoted by η_{SISO}, can be derived. As shown in Fig. 2(b), the power allocated at the reflected resistance R_T^R is the power transferred to the RX, denoted by P_R; from this, the TX efficiency η_T is given by

$$\eta_T = \frac{P_R}{P_{in}} = \frac{R_T^R}{R_T + R_T^R} = \frac{{\omega_r}^2 M^2 / Z_R^{in}}{R_T + {\omega_r}^2 M^2 / Z_R^{in}}. \tag{3}$$

In the same way, the RX efficiency η_R is given by

$$\eta_R = \frac{P_L}{P_R} = \frac{R_L}{R_R + R_L}. \tag{4}$$

Therefore, the overall η_{SISO} is obtained by multiplying η_T and η_R, which is given by

$$\eta_{SISO} = \frac{P_L}{P_{in}} = \frac{{\omega_r}^2 M^2 / Z_R^{in}}{R_T + {\omega_r}^2 M^2 / Z_R^{in}} \frac{R_L}{R_R + R_L}. \tag{5}$$

The derivations above are the most fundamental equations utilized to analyze the WPT. According to 5, the η_{SISO} is highly dependent on the mutual inductance M that indicates the magnetic coupling strength between TX and RX. This indicates that the design of a magnetic coupler that incorporates both the TX and RX coils is critical for improved performance.

2) MIMO-WPT

Fig. 3 is a schematic of a MIMO-WPT configured as n TX coils and m RX coils (*i.e.*, $n \times m$ MIMO-WPT): (a) a general circuit and (b) an equivalent circuit of the TX i and the RX u at the resonant state. Different from the SISO-WPT, a MIMO-WPT has three types of magnetic coupling, as shown in Fig. 3(a): 1) the magnetic coupling between TX i and RX u (M_{iu} and k_{iu}), 2) the cross-coupling between TX i and TX y (M_{Tiy} and k_{Tiy}), and 3) the cross-coupling between RX u and RX v (M_{Ruv} and k_{Ruv}). By considering these additional couplings, (1) and (2) are expanded as follows:

$$Z_{Ru}^{in} I_{Ru} + \sum_{\substack{v=1 \\ v \neq u}}^{m} j\omega M_{Ruv} I_{Rv} = \sum_{i=1}^{n} j\omega M_{iu} I_{Ti}, \tag{6}$$

$$V_{Ti} = R_{Ti} I_{Ti} + \sum_{\substack{y=1 \\ y \neq i}}^{n} j\omega M_{Tiy} I_{Ty} - \sum_{u=1}^{m} j\omega M_{iu} I_{Ru}, \tag{7}$$

where Z_{Ru}^{in} is the input impedance of RX u.

To analyze the MIMO-WPT more conveniently, (6) and (7) can be re-derived using the matrices and vectors listed in Table 1 as follows:

$$\overrightarrow{\mathbf{I_R}} = \mathbf{H}\overrightarrow{\mathbf{I_T}}, \tag{8}$$

$$\overrightarrow{\mathbf{V_T}} = \left(\mathbf{Z_T} + \mathbf{Z_T^R}\right)\overrightarrow{\mathbf{I_T}}, \tag{9}$$

where $\mathbf{H}$ is a magnetic channel that directly connects $\overrightarrow{\mathbf{I_T}}$ and $\overrightarrow{\mathbf{I_R}}$, and $\mathbf{Z_T^R}$ is a matrix of reflected impedance appearing at TX circuit. Here, $\mathbf{H}$ and $\mathbf{Z_T^R}$ are given by

$$\mathbf{H} = j\omega \mathbf{Z_R^{-1}} \mathbf{M}, \tag{10}$$

$$\mathbf{Z_T^R} = \omega^2 \mathbf{M^T} \mathbf{Z_R^{-1}} \mathbf{M}, \tag{11}$$

where the superscript $\mathbf{T}$ and $-\mathbf{1}$ denote a transpose and an inverse of a matrix. The derivation of (10) and (11) are provided in Appendix A.

As shown in Fig. 3(b), the influences of magnetic couplings from other TX and RX to a specific TX i appear as the reflected impedance Z_{Ti}^T and Z_{Ti}^R, which are derived by dividing (7) by I_{Ti} as follows:

$$Z_{Ti}^T = \sum_{\substack{y=1 \\ y \neq i}}^{n} j\omega M_{Tiy} \frac{I_{Ty}}{I_{Ti}}, \tag{12}$$

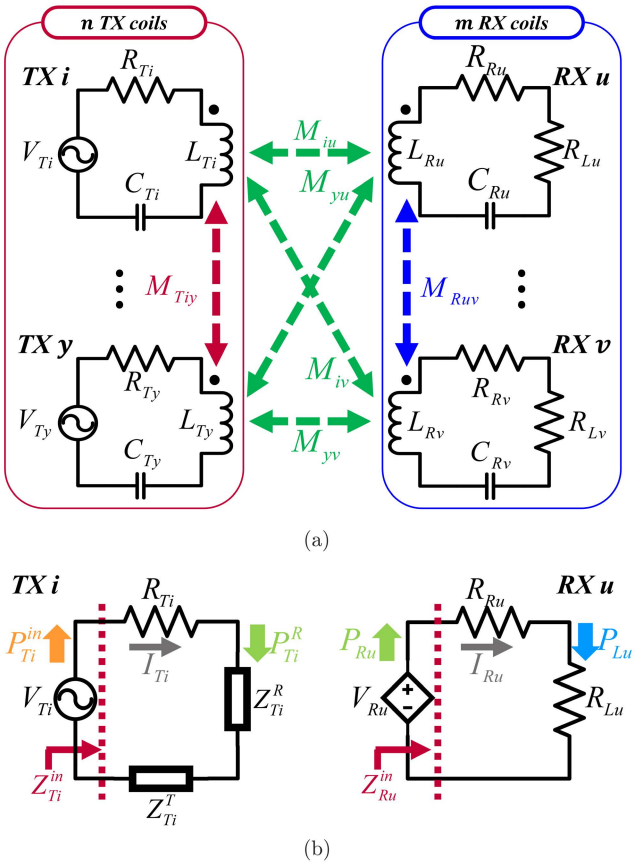

FIGURE 3. Schematic of MIMO-WPT: (a) typical circuit and (b) equivalent circuit at resonant state.

$$Z_{Ti}^{R} = -\sum_{u=1}^{m} j\omega M_{iu} \frac{I_{Ru}}{I_{Ti}}. \tag{13}$$

As a consequence, the input impedance of TX i, denoted by Z_{Ti}^{in}, is given by $Z_{Ti}^{in} = V_{Ti}/I_{Ti} = R_{Ti} + Z_{Ti}^{T} + Z_{Ti}^{R}$.

On the other hand, the influence of magnetic couplings from all TX and other RX to a specific RX u appear as a current-controlled voltage source V_{Ru} (shown in Fig. 3(b)), which is given by

$$V_{Ru} = \sum_{i=1}^{n} j\omega M_{iu} I_{Ti} - \sum_{\substack{v=1 \\ v\neq u}}^{m} j\omega M_{Ruv} I_{Rv}. \tag{14}$$

The first term in (14) is the derived voltage from the TX current $\overrightarrow{\mathbf{I_T}}$ (denoted by V_{Ru}^{T}), and the second term is the derived voltage from the RX current $\overrightarrow{\mathbf{I_R}}$ (denoted by V_{Ru}^{R}). Both induced voltages are connected in series and cause current to flow in the RX circuit.

There is knowledge to consider before deriving the PTE of MIMO-WPT, denoted by η_{MIMO}. Equations (12) and (13) indicate that the input impedance Z_{Ti}^{in}, seen from the voltage source V_{Ti}, is a complex value including resistance and reactance. As a result, the power supplied from the voltage source V_{Ti} is complex power S_{Ti}^{in} divided into active power P_{Ti}^{in} and a reactive power Q_{Ti}^{in} (*i.e.*, $S_{Ti}^{in} = P_{Ti}^{in} + jQ_{Ti}^{in}$) [26]. According to power engineering, the active power (or the real power) is a time average of net transfer energy assigned at the resistance. On the other hand, the reactive power only oscillates between the source and the load, with no net energy transfer to the load [27]. Therefore, the PTE of TX i and of RX u, denoted by η_{Ti} and η_{Ru}, are given by the resistance ratio as follows:

$$\eta_{Ti} = \frac{P_{Ti}^{R}}{P_{Ti}^{in}} = \frac{\mathrm{Re}\left(Z_{Ti}^{R}\right)}{R_{Ti} + \mathrm{Re}\left(Z_{Ti}^{R} + Z_{Ti}^{T}\right)}, \tag{15}$$

$$\eta_{Ru} = \frac{P_{Lu}}{P_{Ru}} = \frac{R_{Lu}}{R_{Ru} + R_{Lu}}, \tag{16}$$

where the term Re is a real component of a complex number. Different from η_{SISO} of (5), η_{MIMO} cannot be easily derived from (15) and (16). It can be derived from the combination of η_{Ti} and η_{Ru} or the ratio of the sum of output active power to the sum of input active power, given by

$$\eta_{MIMO} = \frac{P_L}{P_{in}} = \frac{\sum_{u=1}^{m} P_{Lu}}{\sum_{i=1}^{n} P_{Ti}^{in}}, \tag{17}$$

where P_{Lu} is the power allocated at the load impedance R_{Lu} of RX u, and P_{Ti}^{in} is the input power supplied from the voltage source V_{Ti}, respectively.

TABLE 1. Vector and matrix denotations.

Parameter	Definition
TX voltage $\overrightarrow{\mathbf{V_T}}$	$\begin{bmatrix} V_{T1} & V_{T2} & \cdots & V_{Tn} \end{bmatrix}^{\mathbf{T}}$
TX current $\overrightarrow{\mathbf{I_T}}$	$\begin{bmatrix} I_{T1} & I_{T2} & \cdots & I_{Tn} \end{bmatrix}^{\mathbf{T}}$
RX voltage $\overrightarrow{\mathbf{V_R}}$	$\begin{bmatrix} V_{R1} & V_{R2} & \cdots & V_{Rm} \end{bmatrix}^{\mathbf{T}}$
RX current $\overrightarrow{\mathbf{I_R}}$	$\begin{bmatrix} I_{R1} & I_{R2} & \cdots & I_{Rm} \end{bmatrix}^{\mathbf{T}}$
Mutual inductance $\mathbf{M}$	$\begin{bmatrix} M_{11} & M_{21} & \cdots & M_{n1} \\ \vdots & \vdots & \ddots & \vdots \\ M_{1m} & M_{2m} & \cdots & M_{nm} \end{bmatrix}$
TX impedance $\mathbf{Z_T}$	$\begin{bmatrix} R_{T1} & j\omega M_{T12} & \cdots & j\omega M_{T1n} \\ j\omega M_{T21} & R_{T2} & \cdots & j\omega M_{T2n} \\ \vdots & \vdots & \ddots & \vdots \\ j\omega M_{Tn1} & j\omega M_{Tn2} & \cdots & R_{Tn} \end{bmatrix}$
RX impedance $\mathbf{Z_R}$	$\begin{bmatrix} R_{R1}^{in} & j\omega M_{R12} & \cdots & j\omega M_{R1m} \\ j\omega M_{R21} & R_{R2}^{in} & \cdots & j\omega M_{R2m} \\ \vdots & \vdots & \ddots & \vdots \\ j\omega M_{Rm1} & j\omega M_{Rm2} & \cdots & R_{Rm}^{in} \end{bmatrix}$

In addition to the PTE, there is another indicator for measuring the WPT performance: a PF, denoted by pf. The pf is defined as the ratio of the active power to the apparent power, where the apparent power is an absolute value of complex power S_{Ti}^{in} [26]. According to [1], the pf of the SISO-WPT configured as S-S topology is unity in the magnetically resonant state. This is because the input impedances of the TX and RX circuits are real values, as shown in Fig. 2(b), resulting in all supplied power from the voltage source being active power. However, in the MIMO-WPT, the input impedance Z_{Ti}^{in} is a complex value (shown in Fig. 3(b)). For this reason, the reactive power Q_{Ti}^{in} is supplied from V_{Ti}, causing a variation of pf. Therefore, the PF should be considered, and the PF of TX i, denoted by pf_{Ti}, is given by

$$pf_{Ti} = \frac{P_{Ti}^{in}}{\left|S_{Ti}^{in}\right|} = \frac{\mathrm{Re}\left(Z_{Ti}^{in}\right)}{\left|Z_{Ti}^{in}\right|}. \tag{18}$$

The PF in an AC power system defines how effectively the power input from the source is allocated as active power, which is a different concept than PTE [27]. As a result, when designing and evaluating the MIMO-WPT system, both PTE and PF should be considered.

Notation: For ease of understanding, the list of notation used to describe MIMO-WPT is summarized in Table 2.

B. MAGNETIC BEAMFORMING

Magnetic beamforming, a scheme applicable to a MISO- or MIMO-WPT, focuses the magnetic field from TX coils to the RX location, achieving maximum PTE [11], [12]. This scheme is applied by controlling the TX voltage and current to match the beamforming voltage and current, denoted by $\overrightarrow{\mathbf{V}_{\mathbf{T}}^{\mathbf{bf}}}$ and $\overrightarrow{\mathbf{I}_{\mathbf{T}}^{\mathbf{bf}}}$. The derivations of $\overrightarrow{\mathbf{V}_{\mathbf{T}}^{\mathbf{bf}}}$ and $\overrightarrow{\mathbf{I}_{\mathbf{T}}^{\mathbf{bf}}}$ are explained as follows.

When the total input active power P_{in} (*i.e.*, $P_{in} = \sum P_{Ti}^{in}$) is applied to the MIMO-WPT, P_{in} is distributed at TX and RX circuits as follows:

$$P_{in} = P_T + P_R = \overrightarrow{\mathbf{I}_{\mathbf{T}}}^{*}\mathbf{R}_{\mathbf{T}}\overrightarrow{\mathbf{I}_{\mathbf{T}}} + \overrightarrow{\mathbf{I}_{\mathbf{R}}}^{*}\mathbf{R}_{\mathbf{R}}\overrightarrow{\mathbf{I}_{\mathbf{R}}}, \tag{19}$$

where P_T and P_R are the sums of active power assigned at the TX and RX circuits, and * is a complex conjugate. $\mathbf{R_T}$ and $\mathbf{R_R}$ are $\mathrm{Re}(\mathbf{Z_T})$ and $\mathrm{Re}(\mathbf{Z_R})$, respectively. By substituting (8) into (19), P_{in} is a function of $\overrightarrow{\mathbf{I}_{\mathbf{T}}}$ as follows:

$$P_{in} = P_T + P_R = \overrightarrow{\mathbf{I}_{\mathbf{T}}}^{*}\mathbf{R}_{\mathbf{T}}\overrightarrow{\mathbf{I}_{\mathbf{T}}} + \overrightarrow{\mathbf{I}_{\mathbf{T}}}^{*}\mathbf{H}^{*}\mathbf{R}_{\mathbf{R}}\mathbf{H}\overrightarrow{\mathbf{I}_{\mathbf{T}}}. \tag{20}$$

As explained, magnetic beamforming achieves the maximum P_R under the constraint of P_{in}. Thus, the beamforming current $\overrightarrow{\mathbf{I}_{\mathbf{T}}^{\mathbf{bf}}}$ is given by: $\overrightarrow{\mathbf{I}_{\mathbf{T}}^{\mathbf{bf}}} = \mathrm{argmax}\left(\overrightarrow{\mathbf{I}_{\mathbf{T}}}^{*}\mathbf{H}^{*}\mathbf{R}_{\mathbf{R}}\mathbf{H}\overrightarrow{\mathbf{I}_{\mathbf{T}}}\right)$, where the constraint is P_{in} of (19).

According to [12], the beamforming current $\overrightarrow{\mathbf{I}_{\mathbf{T}}^{\mathbf{bf}}}$ can be calculated via convex optimization, which is given by

$$\overrightarrow{\mathbf{I}_{\mathbf{T}}^{\mathbf{bf}}} = c\ maxeig\left(\mathbf{H}^{*}\mathbf{R}_{R}\mathbf{H}\right), \tag{21}$$

TABLE 2. List of notation for MIMO-WPT.

Notation	Definition
n and m	The number of TX and RX coils
P_{Ti}^{in}, Q_{Ti}^{in}, and S_{Ti}^{in}	Input active power, reactive power, and apparent power supplied from voltage source V_{Ti}
P_{in}	Total input active power ($\sum_{i=1}^{n} P_{Ti}^{in}$)
P_{Lu}	Output power allocated at R_{Lu} of RX u
P_L	Total output power ($\sum_{u=1}^{m} P_{Lu}$)
Z_{Ti}^{T}	Reflected impedance from other TXs to TX i
Z_{Ti}^{T}	Reflected impedance from other TXs to TX i
Z_{Ti}^{R}	Reflected impedance from all RXs to TX i
Z_{Ti}^{T}	Reflected impedance from other TXs to TX i
Z_{Ti}^{in} and Z_{Ru}^{in}	Input impedance of TX i and RX u
V_{Ru}^{T}	Induced voltage from all TXs to RX u
V_{Ru}^{R}	Induced voltage from other RXs to RX u
M_{iu}	Mutual inductance between TX i and RX u (Magnetic couplings between TX and RX array)
M_{Tiy}	Mutual inductance between TX i and TX y (Cross-couplings in TX array)
M_{Ruv}	Mutual inductance between RX u and RX v (Cross-couplings in RX array)
η_{Ti} and η_{Ru}	PTE of TX i and RX u
pf_{Ti}	PF of TX i
η_{MIMO}	PTE of MIMO-WPT
pf_{MIMO}	PF of MIMO-WPT

where *maxeig* is an eigenvector v_{max} of $\mathbf{H}^{*}\mathbf{R_R}\mathbf{H}$ that satisfies the largest real eigenvalue λ_{max} (*i.e.*, $(\mathbf{H}^{*}\mathbf{R_R}\mathbf{H})\ v_{max} = \lambda_{max}\ v_{max}$), and c is a constant determined by P_{in}. The beamforming voltage $\overrightarrow{\mathbf{V}_{\mathbf{T}}^{\mathbf{bf}}}$ is given by substituting (21) into (9).

Here is a summary of magnetic beamforming. The beamforming current $\overrightarrow{\mathbf{I}_{\mathbf{T}}^{\mathbf{bf}}}$ calculated by (21) flows in the TX circuits when the beamforming voltage $\overrightarrow{\mathbf{V}_{\mathbf{T}}^{\mathbf{bf}}}$ is applied to the MISO- or MIMO-WPT. Under the constraint of P_{in}, the magnetic fields generated by the beamforming currents are concentrated at the RX location, transmitting the maximum P_R to the RX circuits, and resulting in the maximum PTE. A detailed description of magnetic beamforming is provided in [11] and [12].

III. ANALYSIS ON MAGNETIC COUPLINGS IN MIMO-WPT

This section provides closed form solutions for two RX coils with multiple n TX coils (*i.e.*, $n \times 2$ MIMO-WPT). Furthermore, a numerical analysis of a MIMO-WPT with more

than three RX coils is presented because deriving the inverse matrix of $\mathbf{Z_R}$ in (10) is not feasible for more than three RX coils due to high mathematical complexity.

A. THEORETICAL ANALYSIS

1) BEAMFORMING CURRENT EQUATION FOR $n \times 2$ MIMO-WPT

According to [15], the beamforming current $\overrightarrow{\mathbf{I_T^{bf}}}$ of a MISO-WPT having multiple TX coils and a single RX coil is proportional to the mutual inductance $\mathbf{M}$ between each TX and RX coil. In Appendix B, we derive a simple beamforming current equation for $n \times 2$ MIMO-WPT having two RX coils with the same value of resistance and inductance (*i.e.*, $R_R^{in} = R_{R1}^{in} = R_{R2}^{in}$ and $L_R = L_{R1} = L_{R2}$). The derived equation is as follows:

$$\overrightarrow{\mathbf{I_T^{bf}}} = c' \, maxeig\left(\mathbf{M}^*\mathbf{M}\right), \tag{22}$$

The constant c' is determined by the constraint of P_{in} or calculated using $c' = c\omega^2/det(\mathbf{Z_R})$, where *det* is a determinant of a matrix.

Equation (22) provides the properties of the beamforming current $\overrightarrow{\mathbf{I_T^{bf}}}$. The ratio of beamforming current, not its absolute amplitude, is solely determined by the mutual inductance $\mathbf{M}$ between TX and RX coils, regardless of the other cross-couplings $\mathbf{M_T}$ and $\mathbf{M_R}$ ($\mathbf{M_T}$ and $\mathbf{M_R}$ denote the sets of mutual inductance M_{Tiu} and M_{Ruv}, respectively). This allows the beamforming current $\overrightarrow{\mathbf{I_T^{bf}}}$ to be calculated simply by estimating the mutual inductance $\mathbf{M}$. Furthermore, all the beamforming currents are positive real values. This is because the eigenvector v_{max} of a non-negative matrix $\mathbf{H}^*\mathbf{R_R}\mathbf{H}$, which corresponds to the largest eigenvalue λ_{max}, has all non-negative components due to the Perron-Frobenius theorem [28]. As a result, the beamforming currents flowing in the TX circuits are all in phase.

Based on the equivalent circuits and derived equations above, the influences of all the magnetic couplings that occur in the MIMO-WPT when applying magnetic beamforming are examined below.

2) EQUIVALENT CIRCUIT ANALYSIS OF $n \times 2$ MIMO-WPT WITH MAGNETIC BEAMFORMING

As shown in Fig. 3(b), the influences of all magnetic couplings in MIMO-WPT emerge as the reflected impedance Z_{Ti}^T and Z_{Ti}^R, and the induced voltage V_{Ru} at equivalent TX circuit and RX circuit, respectively. Therefore, these magnetic couplings can be examined theoretically through equivalent circuit analysis. It is necessary to make the reflected impedance Z_{Ti}^T and Z_{Ti}^R, and the induced voltage V_{Ru} as a function of the TX currents $\overrightarrow{\mathbf{I_T}}$ to derive the influences of magnetic couplings when applying magnetic beamforming. This is because magnetic beamforming requires adjustment of the TX current to the beamforming current $\overrightarrow{\mathbf{I_T^{bf}}}$. For simple analysis, we assume that the MIMO-WPT is configured as TX and RX circuits having identical components (*i.e.*, $R_R = R_T$, $L_R = L_T$, and $C_R = C_T$), and that the load impedance of all RX circuit is identical (*i.e.*, $R_L = R_{L1} = R_{L2}$).

For theoretical analysis, a magnetic channel $\mathbf{H}$ of (10) should be algebraically analyzed to replace the $\overrightarrow{\mathbf{I_R}}$ with $\overrightarrow{\mathbf{I_T}}$. Substituting $\mathbf{H}$ of (10) into $\overrightarrow{\mathbf{I_R}}$ of (8), I_{R1} and I_{R2} are given by

$$I_{R1} = \frac{1}{det\left(\mathbf{Z_R}\right)} \sum_{i=1}^{n} \left(\omega^2 M_{i2} M_{R12} + j\omega M_{i1} R_R^{in}\right) I_{Ti}, \tag{23}$$

where $det\left(\mathbf{Z_R}\right) = \omega^2 {M_{R12}}^2 + {R_R^{in}}^2$ and $R_R^{in} = R_R + R_L$. The RX current I_{R2} is given by replacing 1 with 2 in (23). By substituting (23) into (13), the reflected impedance Z_{Ti}^R is divided into the reflected resistance R_{Ti}^R and reflected reactance X_{Ti}^R as follows:

$$R_{Ti}^R = \frac{R_R^{in}}{det\left(\mathbf{Z_R}\right)} \left[\sum_{\substack{y=1 \\ y\neq i}}^{n} \left(\sum_{u=1}^{2} \omega^2 M_{iu} M_{yu} \frac{I_{Ty}}{I_{Ti}}\right)\right], \tag{24}$$

$$X_{Ti}^R = -\frac{\omega M_{R12}}{det\left(\mathbf{Z_R}\right)} \left[\sum_{u=1}^{2} \omega^2 M_{iu} \alpha_u\right], \tag{25}$$

where α_u is defined as $\alpha_1 = \sum_{\substack{y=1 \\ y\neq i}}^{n} M_{i2} I_{Ty}/I_{Ti}$ and $\alpha_2 = \sum_{\substack{y=1 \\ y\neq i}}^{n} M_{i1} I_{Ty}/I_{Ti}$. As explained, the beamforming current $\overrightarrow{\mathbf{I_T^{bf}}}$ of $n \times 2$ MIMO-WPT is always in phase; therefore, substituting in-phase $\overrightarrow{\mathbf{I_T^{bf}}}$ into (24) and (25), R_{Ti}^R and X_{Ti}^R become pure resistance and capacitance, respectively. That is, the reflected impedance Z_{Ti}^R consists of the reflected resistance R_{Ti}^R and the reflected capacitance X_{Ti}^R when magnetic beamforming is applied. Here, the power allocated at the reflected resistance R_{Ti}^R is the power wirelessly transferred to the two RX coils from TX i, denoted by P_{Ti}^R in Fig. 3(b).

In the same way as above, the reflected impedance Z_{Ti}^T of (12) becomes a pure inductance X_{Ti}^T due to in-phase $\overrightarrow{\mathbf{I_T^{bf}}}$, which is given by

$$X_{Ti}^T = \sum_{\substack{y=1 \\ y\neq i}}^{n} j\omega M_{Tiy} \frac{I_{Ty}}{I_{Ti}}. \tag{26}$$

Equation (26) indicates that the reflected impedance Z_{Ti}^T has no resistance component when magnetic beamforming is applied.

On the other hand, the induced voltage source V_{R1} is given by $V_{R1} = V_{R1}^T + V_{R1}^R$, where V_{R1}^T and V_{R1}^R are

$$V_{R1}^T = \sum_{i=1}^{n} j\omega M_{i1} I_{Ti}, \tag{27}$$

$$V_{R1}^R = -\frac{\omega M_{R12}}{det\left(\mathbf{Z_R}\right)} \sum_{i=1}^{n} \left(\omega M_{i2} R_R^{in} - j\omega^2 M_{i1} M_{R12}\right) I_{Ti}. \tag{28}$$

V_{R2} is obtained by replacing 1 with 2 in (27) and (28).

Based on the derivations above, the equivalent circuits of TX and RX in Fig. 3(b) are altered to those in Fig. 4,

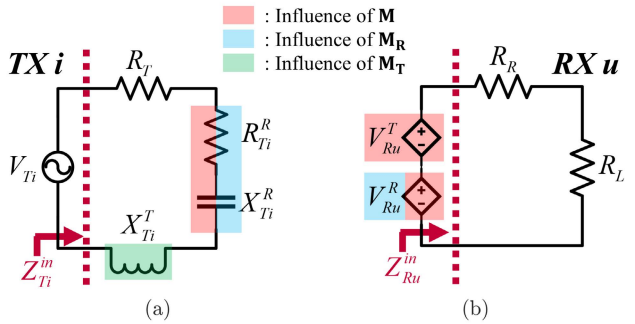

FIGURE 4. Equivalent circuit of MIMO-WPT under magnetic beamforming status: (a) TX *i* and (b) RX *u*.

when magnetic beamforming is applied. In summary, when magnetic beamforming is applied to $n \times 2$ MIMO-WPT, the equivalent circuit of TX becomes a series *RLC* circuit composed of two resistances R_T and R_{Ti}^R, one inductance X_{Ti}^T, and one capacitance X_{Ti}^R. Additionally, the equivalent circuit of the RX has one induced voltage source V_{Ru} composed of the serially connected V_{Ru}^T and V_{Ru}^R.

3) INFLUENCES OF MAGNETIC COUPLINGS ON THE PTE AND PF

a: **M***: MAGNETIC COUPLINGS BETWEEN TX AND RX ARRAYS*

In general, the mutual inductance **M**, which depends on the coil specification and the relative distance between TX and RX arrays, has the most significant impact on determining the WPT performance [8]; therefore, elaborate design of the magnetic coupler is essential. This property is also applicable to magnetic beamforming.

First, the mutual inductance **M** is the most decisive factor for the beamforming current $\overrightarrow{\mathbf{I}_\mathbf{T}^{\mathbf{bf}}}$. According to (22), **M** determines the ratio of beamforming current, while the total input power P_{in} determines its amplitude. In other words, because the coil specification and the total input power P_{in} are fixed once set, the relative distance between both arrays is the decisive factor for beamforming current.

Next, the reflected impedance Z_{Ti}^R and the induced voltage V_{Ru} are a function of **M**, as shown in Fig. 4. We compared two cases for ease of analysis on **M**: the specific **M** and $d\mathbf{M}$ (d is a positive real value). According to (22), both **M** and $d\mathbf{M}$ have the same ratio of beamforming current. This is because the unit eigenvectors of **M** and $d\mathbf{M}$ are the same according to linear algebra [29]. For this reason, I_{Ty}/I_{Ti} in (24) and (25) can be replaced by a constant in both cases. As a result, it can be known that R_{Ti}^R and X_{Ti}^R are proportional to the square of d by substituting $d\mathbf{M}$ into (24) and (25). This confirms that, as **M** increases ($d > 1$) or decreases ($d < 1$), R_{Ti}^R and X_{Ti}^R increases or decreases, respectively.

Based on the above analyses, the influences of **M** on the PTE and PF can be theoretically derived. As explained, the reflected resistance R_{Ti}^R and reflected capacitance X_{Ti}^R increase as **M** increases. In terms of the PTE, an increase in R_{Ti}^R improves η_{Ti} of (15). Because η_{Ru} is a constant value once set, increasing η_{Ti} leads to an improved overall PTE η_{MIMO}. On the other hand, the relationship between pf_{Ti} and **M** requires calculation. This is because the numerator of pf_{Ti} contains only R_{Ti}^R, while the denominator contains both R_{Ti}^R and X_{Ti}^R, respectively, as shown in (18). In conclusion, **M** is proportional to the PTE when magnetic beamforming is applied, but the calculation is required to derive the PF due to the complicated relationship.

b: $\mathbf{M_T}$*: CROSS-COUPLINGS AT TX ARRAY*

When multiple TX coils are arranged to extend the wireless charging range, the mutual inductance $\mathbf{M_T}$, indicating the cross-coupling at TX coils, inevitably emerges. Prior studies have reported that $\mathbf{M_T}$ causes the leakage fields, which leads to performance degradation [10], [13]. Based on these studies, it is expected that $\mathbf{M_T}$ at the TX coils worsens the PTE and PF. However, $\mathbf{M_T}$ worsens the PF but has no effect on the PTE when magnetic beamforming is applied. This is because, as shown in Fig. 4(a), the reflected impedance Z_{Ti}^T of (26) emerges only as the reflected inductance X_{Ti}^T at the equivalent TX circuit when magnetic beamforming is applied. For this reason, η_{Ti} of (15) as determined by the resistance ratio, is unaffected, while pf_{Ti} of (18) is affected by an increase in its denominator. The term pf_{Ti} decays as $\mathbf{M_T}$ increases, indicating that more apparent power is required to supply the same amount of active power. In addition, $\mathbf{M_T}$ has no influence on the RX circuits when magnetic beamforming is applied, as shown in Fig. 4(b).

Meanwhile, $\mathbf{M_T}$ increases the amplitude of beamforming voltage $\overrightarrow{\mathbf{V}_\mathbf{T}^{\mathbf{bf}}}$ that drives the beamforming current $\overrightarrow{\mathbf{I}_\mathbf{T}^{\mathbf{bf}}}$. As $\mathbf{M_T}$ increases, the magnitude of input impedance Z_{Ti}^{in} (denoted by $|Z_{Ti}^{in}|$) increases according to (12). Because $\overrightarrow{\mathbf{I}_\mathbf{T}^{\mathbf{bf}}}$ is independent of $\mathbf{M_T}$, an increase in $\mathbf{M_T}$ directly increases the amplitude of $\overrightarrow{\mathbf{V}_\mathbf{T}^{\mathbf{bf}}}$ according to (9). This indicates that as $\mathbf{M_T}$ increases, a higher voltage is necessary to supply the beamforming current of the same amplitude; therefore, the components in TX circuits must withstand high voltage, meaning increased cost.

c: $\mathbf{M_R}$*: CROSS-COUPLINGS AT RX ARRAY*

The mutual inductance $\mathbf{M_R}$, indicating the cross-couplings at RX coils, must be considered when the WPT is configured as multiple TX and RX coils. Similar to **M**, $\mathbf{M_R}$ influences both the PTE and PF when magnetic beamforming is applied. This is because $\mathbf{M_R}$ affects the reflected resistance R_{Ti}^R and reflected capacitance X_{Ti}^R, as shown in Fig. 4(a). However, unlike **M**, which is proportional to the PTE, an increase in $\mathbf{M_R}$ lowers the reflected resistance R_{Ti}^R of (24), reducing η_{Ti}. This is equivalent to the case that increased $\mathbf{M_R}$ weakens the magnetic coupling strength between the TX and RX, thereby inhibiting power transmission. On the other hand, the reflected reactance X_{Ti}^R fluctuates depending on $\mathbf{M_R}$. This is because the denominator and numerator of X_{Ti}^R in (25) are both composed of a function of $\mathbf{M_R}$. For this reason, the

TABLE 3. Summary of theoretical analysis.

Type of Couplings	Variation in TX i	PTE η_{Ti}	PF pf_{Ti}
$\mathbf{M}\uparrow$	Resistance $R^R_{Ti}\uparrow$	$\uparrow$	$\uparrow$
	Capacitance $X^R_{Ti}\uparrow$	-	$\downarrow$
$\mathbf{M_T}\uparrow$	Inductance $X^T_{Ti}\uparrow$	-	$\downarrow$
$\mathbf{M_R}\uparrow$	Resistance $R^R_{Ti}\downarrow$	$\downarrow$	$\downarrow$
	Capacitance $X^R_{Ti}\uparrow\downarrow$	-	$\uparrow\downarrow$

A PF of 1.0 is achieved when the magnitude of X^R_{Ti} and X^T_{Ti} have the same magnitude ($i.e.$, $|X^R_{Ti}|=|X^T_{Ti}|$) or when $\mathbf{M_T}$ and $\mathbf{M_R}$ are zero ($i.e.$, $\mathbf{M_T}=\mathbf{M_R}=0$). The symbol $\uparrow\downarrow$ denotes that it is a concave function, not a monotonic increase or decreases.

influence of $\mathbf{M_R}$ on the PF requires calculation, the same as for $\mathbf{M}$.

Table 3 shows a summary of the theoretical analysis. In consequence, when using magnetic beamforming in the MIMO-WPT, $\mathbf{M}$ should be increased, and $\mathbf{M_R}$ should be minimized to boost the PTE, but the PTE is unaffected by $\mathbf{M_T}$. Additionally, $\mathbf{M_T}$ and $\mathbf{M_R}$ generate a reflected inductance and capacitance, respectively, in the TX equivalent circuit, attenuating the PF. Therefore, it is necessary to increase $\mathbf{M}$ and reduce $\mathbf{M_T}$ and $\mathbf{M_R}$ for a higher PTE and PF in MIMO-WPT.

4) ADVANTAGES OF MAGNETICALLY INDEPENDENT TX AND RX ARRAYS

Based on the analyses of $\mathbf{M}$, $\mathbf{M_R}$, and $\mathbf{M_T}$, the advantages of magnetically independent TX and RX arrays ($i.e.$, $\mathbf{M_T}$ and $\mathbf{M_R}$ are zero) can be derived. Fig. 5 shows an equivalent circuit of MIMO-WPT using the magnetically independent TX and RX array: (a) TX i and (b) RX u.

Regarding the TX circuit, the reflected inductance X^T_{Ti} and reflected capacitance X^R_{Ti} are eliminated when both TX and RX arrays are magnetically independent, resulting in a PF of 1.0. This indicates no reactive power circulating in the TX circuit and that all the apparent power supplied is active power. In addition, operation with low beamforming voltage $\overrightarrow{\mathbf{V}}^{\mathbf{bf}}_{\mathbf{T}}$ is possible. This is because the magnitude of the input impedance, $|Z^{in}_{Ti}|$, decreases due to the eliminated imaginary part of the input impedance Z^{in}_{Ti} when $\mathbf{M_T}$ and $\mathbf{M_R}$ are removed. Furthermore, the reflected resistance R^R_{Ti} of (24) changes as follows:

$$R^R_{Ti}=\frac{1}{R^{in}_R}\left[\sum_{\substack{y=1\\y\neq i}}^{n}\left(\sum_{u=1}^{2}\omega^2 M_{iu}M_{yu}\frac{I_{Ty}}{I_{Ti}}\right)\right]. \tag{29}$$

Comparing (24) and (29) shows that removing $\mathbf{M_R}$ provides the maximum reflected resistance R^R_{Ti}, resulting in the highest η_{Ti} when $\mathbf{M}$ is fixed at a specific value. In addition, (29) indicates that η_{Ti} is absolutely a function of $\mathbf{M}$ when magnetic beamforming is applied. This is because R^{in}_R of (29) is a fixed constant once specified, and the beamforming current $\overrightarrow{\mathbf{I}}^{\mathbf{bf}}_{\mathbf{T}}$ is also a function of $\mathbf{M}$, as explained in (22).

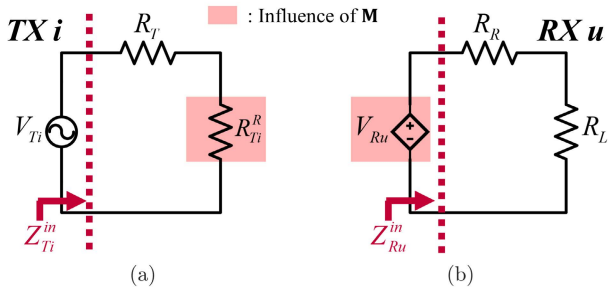

FIGURE 5. Equivalent circuit of MIMO-WPT using magnetically independent TX and RX arrays: (a) TX *i* and (b) RX *u*.

As a consequence, when the TX and RX arrays are magnetically independent, the PTE η_{Ti} under magnetic beamforming is only determined by $\mathbf{M}$ once other parameters are fixed. This can be seen from the fact that R^R_{Ti} in Fig. 5(a) is determined only by $\mathbf{M}$. This makes the PTE calculation of the MIMO-WPT much simpler, similar to that of the SISO-WPT in (3)−(5). From the RX perspective, the induced voltage V_{Ru} is only determined by $\mathbf{M}$, without being interfered with by other RX coil. This makes it easy to calculate the current and power transferred to the RX coils.

B. NUMERICAL ANALYSIS VIA MATLAB

A numerical analysis was carried out to supplement the theoretical analysis above. We set a 3 × 3 MIMO-WPT with three TX coils and three RX coils, as shown in Fig. 6. The parameters for analysis are listed in Table 4. We used the coupling coefficient instead of the mutual inductance to specify the magnetic coupling strength as a normalized value. To consider the scenario where the distance between TX and RX arrays varies, we set three cases depending on the critical coupling k_c: 1) under-coupled when $k < k_c$, 2) critical-coupled when $k = k_c$, and 3) over-coupled when $k > k_c$. The critical coupling k_c is defined as $k_c = 1/\sqrt{Q_T Q_R}$, where Q_T and Q_R are the quality factor of L_T and L_R [30]. For simple analysis, 1) under-coupled and 3) over-coupled cases were set by multiplying k_c by a random number uniformly distributed in the interval [0.5,1] and [1,1.5], respectively. That is, in 2) critical-coupled case, all the coupling coefficient k between each pair of TX and RX coils are the same value as the critical coupling k_c. In the other two cases, each TX coil has a different coupling coefficient k. We executed 100 iterations to evaluate as many results as possible with a different random number in 1) under-coupled and 3) over-coupled cases. Then, we compared the maximum, minimum, and average results of the two cases to the critical-coupled case results. In addition, for simple analysis, k_T and k_R are equally adjusted from 0 to 0.2 in all cases ($i.e.$, $k_T = k_{T12} = k_{T23} = k_{T31}$ and $k_R = k_{R12} = k_{R13} = k_{R31}$).

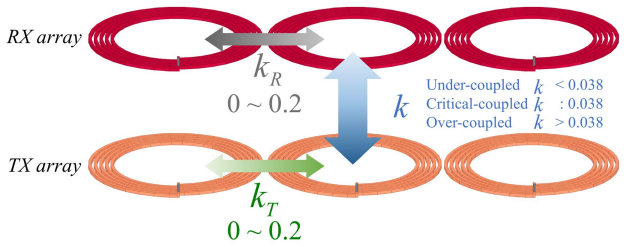

FIGURE 6. Concept of 3 × 3 MIMO-WPT for numerical analysis.

TABLE 4. Parameters of numerical analysis for 3 × 3 MIMO-WPT.

Parameter	Value	Description
Resonant frequency f_r	85 kHz	
Intrinsic resistance R_T, R_R	0.2 Ω	
Load impedance R_L	5 Ω	
Self inductance L_T, L_R	50 μH	
Coupling coefficient k	$\left[k_c\right]_{3\times3}$.× $[\mathrm{rand}(0.5, 1)]_{3\times3}$	1) Under-coupled
	$\left[k_c\right]_{3\times3}$	2) Critical-coupled
	$\left[k_c\right]_{3\times3}$.× $[\mathrm{rand}(1, 1.5)]_{3\times3}$	3) Over-coupled
Coupling coefficient k_T	$0 \sim 0.2$	
Coupling coefficient k_R	$0 \sim 0.2$	
Total input active power P_{in}	50 W	
Iteration count (Case-2, 3)	100	

The critical coupling k_c is 0.038, and the term rand(a,b) is uniformly distributed random number in the interval (a,b). The term .× is an element-wise multiplication of matrix.

Fig. 7 shows a PTE η_{MIMO} depending on k_T and k_R: (a) η_{MIMO} when k_T is adjusted from 0 to 0.2 and k_R is 0 and (b) η_{MIMO} when k_R is adjusted from 0 to 0.2 and k_T is 0. The variation bar at each point of the over-coupled and under-coupled cases indicates the maximum and minimum values for an iteration, while the line represents the average value. As shown in Fig. 7(a), the average η_{MIMO} increases from 80 % to 90 % when k increases from under-coupled to over-coupled. However, η_{MIMO} is determined regardless of k_T at each case. This is because the influence of cross-coupling at TX coils emerges only as a reflected inductance independent of η_{MIMO}, as explained previously.

Meanwhile, both k and k_R affect η_{MIMO}, as shown in Fig. 7(b). The over-coupled case has the highest average η_{MIMO} of all the cases, and there is no intersection point of η_{MIMO} with the other cases when k_R is adjusted from 0 to 0.2. In addition, the minimum point of the over-coupled case extracted through the variation bar is higher than that of the other cases. This result indicates that the charging distance between TX and RX coils has a decisive impact in η_{MIMO}. On the other hand, η_{MIMO} is continuously reduced as k_R increases from 0 to 0.2. This result is because an increased k_R weakens the magnetic coupling strength between TX and

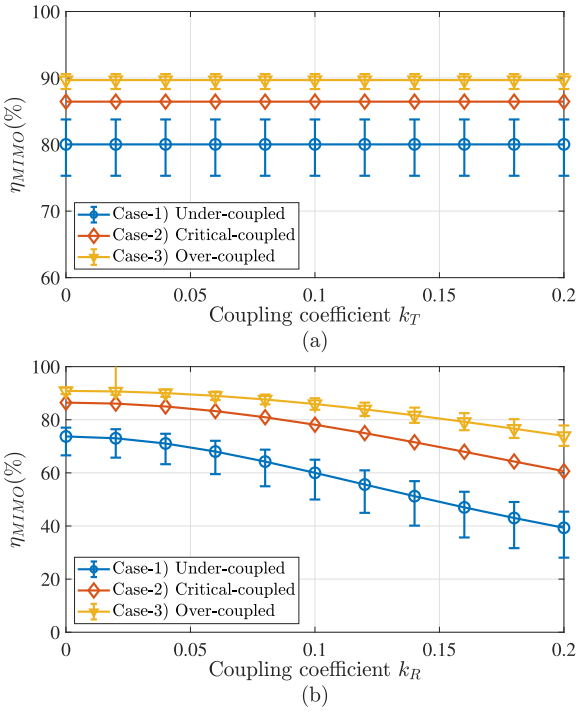

FIGURE 7. PTE η_{MIMO}: (a) η_{MIMO} when k_T varies from 0 to 0.2 and (b) η_{MIMO} when k_R varies from 0 to 0.2.

RX coils, as explained previously. Furthermore, the PTE attenuation caused by k_R is more pronounced as k is lowered. While k_R is adjusted from 0 to 0.2, η_{MIMO} attenuation of over-coupled, critical-coupled, and under-coupled cases are about 17 %, 26 %, and 34 %, respectively.

Fig. 8 shows a PF pf_{MIMO}, an average of pf_{Ti}, depending on k_T and k_R (the maximum and minimum values are omitted, and only the average value is displayed): (a) under-coupled, (b) critical-coupled, and (c) over-coupled. The results of three cases show pf_{MIMO} is affected by all of the magnetic couplings in MIMO-WPT: k_T, k_R, and k. The results show that the influences of these magnetic couplings are the same as the theoretical analysis of MIMO-WPT having two RX coils.

First, k_T significantly attenuates pf_{MIMO}. As k_T increases from 0 to 0.2, pf_{MIMO} of all cases gradually attenuates to 0. This is because the reflected inductance X_{Ti}^T, which attenuates pf_{MIMO}, is linearly proportional to k_T according to (26). Next, pf_{MIMO} increases as k increases, which is evidently shown by comparing the area where pf_{MIMO} is higher than 0 in the three cases. In the over-coupled case, pf_{MIMO} remains above 0.8 until about 0.05 of k_T, as indicated by the red color in Fig. 8(c). However, in the under-coupled case, the area of pf_{MIMO} $\geq$0.8 sharply decreases as k_T increases, as shown in Fig. 8(a). This comparison indicates that the closer the charging distance, the pf_{MIMO} is less affected by k_T. This is because an increase in k increases the reflected resistance at each TX equivalent circuit; therefore, the real part of the numerator and the denominator of pf_{Ti} in (18) increases. Thus, it consequently contributes to increasing the overall pf_{MIMO}. In all cases, there are combinations of k_T and k_R that achieve a pf_{MIMO} of 1.0, which is the highest value of the

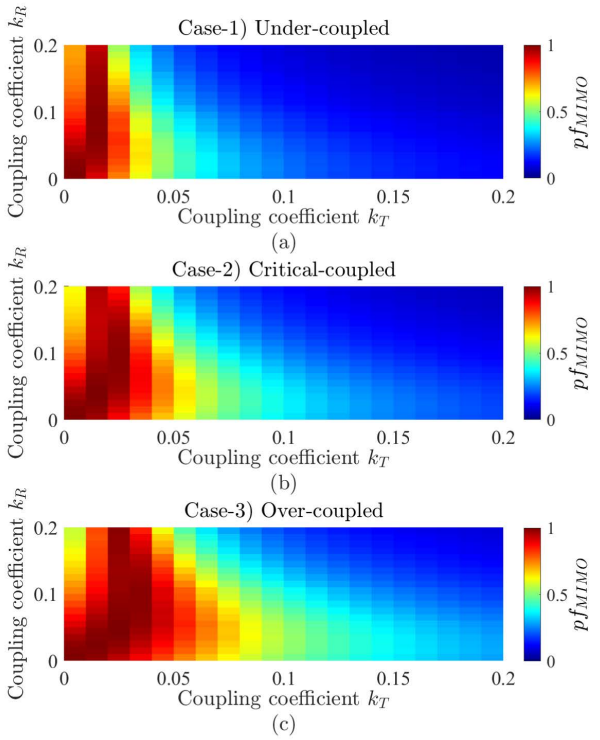

FIGURE 8. PF pf_{MIMO}: (a) under-coupled, (b) critical-coupled, and (c) over-coupled.

PF. The first point is a combination where both k_T and k_R are eliminated (*i.e.*, $k_R = k_T = 0$), which indicates that the TX and RX arrays are magnetically independent. The first point can be achieved regardless of k. The second point is a combination where the reflected inductance and capacitance are canceled out by the same magnitude. However, the second point depends on k, so it is difficult to achieve pf_{MIMO} of 1.0 by satisfying this combination.

Based on the numerical analysis, the influences of k, k_T, and k_R on the PTE and PF of the MIMO-WPT with three RX coils are confirmed. The results show that the above theoretical analysis can be applied to many more RX coils than three. The PTE is proportional to k and inversely proportional to k_R. The PF is determined by k, k_T, and k_R. Based on theoretical and numerical analysis, the criteria of a magnetic coupler for higher PTE and PF of a MIMO-WPT applying magnetic beamforming are as follows: elimination of k_T and k_R, and an increase of k.

IV. PROPOSAL FOR A MODULAR COIL ARRAY

Thus far, we have derived the criteria of $\mathbf{M}$, $\mathbf{M_T}$, and $\mathbf{M_R}$ for improving PTE and PF when applying magnetic beamforming to MIMO-WPT. Section IV proposes a modular coil array, a magnetic coupler that satisfies the above-derived criteria.

A. BASIS SQUARE COIL FOR MIMO-WPT

According to [4] and [31], a rectangular or square coil has a larger coupling area than circular or elliptical coils with the same horizontal and vertical dimensions; thus, these forms are most widely used in WPT for EV charging [32]. For this reason, we chose a square coil as the basis for designing the MIMO-WPT, as shown in Fig. 9: (a) single square coil and (b) square coil array. A specification of the basis square coil is as follows: 1) it is made of copper, 2) the overall width and height are both 60 cm, and 3) the thickness, width, and space of each copper line are 10, 10, and 5 mm, respectively. The self-inductance and intrinsic resistance derived using HFSS are 24 μH and 0.2 Ω. Fig. 9(b) is a square coil array configured as three coils. The gap between each coil is 5 mm. The derived coupling coefficient between adjacent coils is 0.1 (*i.e.*, $k_{T12} = k_{T23} = 0.1$), while k_{T31} is 0.

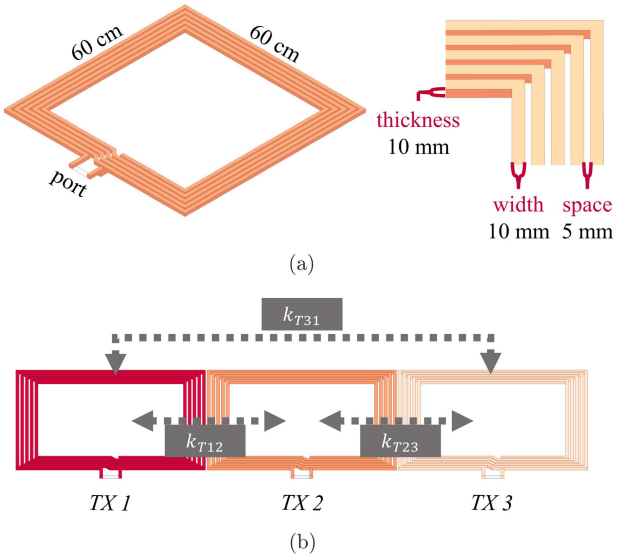

FIGURE 9. Basis square coil for WPT: (a) single square coil and (b) square coil array for MIMO-WPT.

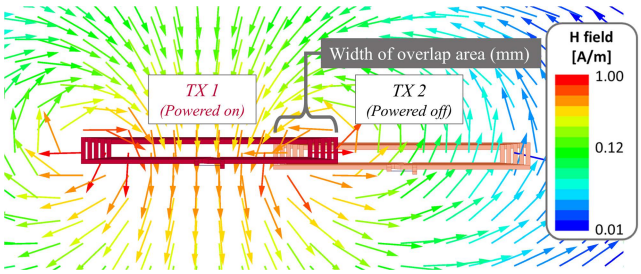

FIGURE 10. Magnetic field distribution when the two coils are deployed in a BP arrangement.

B. FLUX CANCELLATION BY BP ARRANGEMENT

As shown in Fig. 9(b), cross-coupling between adjacent coils inevitably emerges when an array is composed of multiple coils. This phenomenon causes many problems while transferring power. A bipolar (BP) arrangement, partially overlapping each coil to another coil, is a great way to solve the cross-coupling problem [33], [34]. Fig. 10 shows a magnetic field distribution when the two coils are placed in a BP

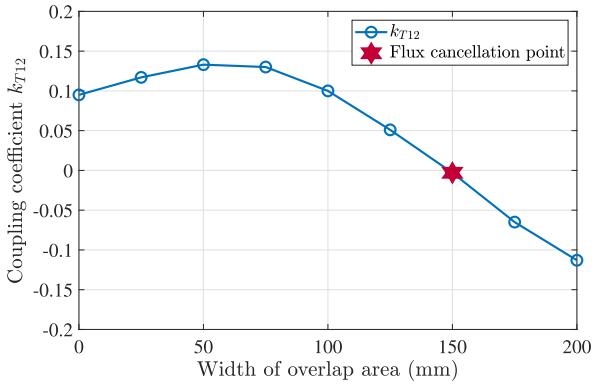

FIGURE 11. Coupling coefficient k_{T12} between TX 1 and TX 2 in Fig 10.

arrangement, where both coils are magnetically decoupled (TX 1 is powered and TX 2 is not powered). This magnetic decoupling occurs due to flux cancellation between coils. As shown in Fig. 10, when two coils partially overlap in a specific area, the downward magnetic flux induced by TX 1 that penetrates TX 2 is canceled out by the upward-directed magnetic flux induced by TX 1. As a result, the net flux linkage between two coils is zero, resulting in no magnetic coupling between them [2]. Because the shape of the coil determines the extent of the overlap area causing a zero magnetic coupling, it is appropriate to utilize the FEM simulation to find the specific overlap area that satisfies the BP arrangement.

Fig. 11 shows the coupling coefficient k_{T12} between two adjacent coils TX 1 and TX 2 in Fig. 10 as the width of overlap area varies. The flux cancellation point where two coils are magnetically separated is around 150 mm. At this point, the two coils are magnetically decoupled, allowing them to be driven independently without interference from another coil.

C. MODULAR COIL ARRAY BASED ON THE BP ARRANGEMENT

1) DESIGN CONCEPT

a: DISADVANTAGES OF THE BP ARRANGEMENT

Despite its outstanding efficacy in reducing cross-coupling between adjacent coils, the BP arrangement has drawbacks. To begin with, insulation between overlapping coils is a non-negligible concern in practical use [9]. When two coils come into physical contact, the characteristic of each coil completely changes, causing performance variation. Furthermore, in terms of scalability, it is difficult to configure a BP arrangement with more than two coils by placing multiple coils at the exact flux cancellation point. As a result, many studies of BP arrangements are limited to two coils, as the term ''bipolar'' implies.

Meanwhile, the surface of the BP arrangement is not flat due to the height difference between the two coils. Because of the non-flat property, an empty gap occurs when the BP arrangement is placed over materials of ferrite or aluminum (components of a typical WPT system) or under such materials as acrylic or glass plates for protection. As a result, the thickness grows, and the ability to withstand weakens.

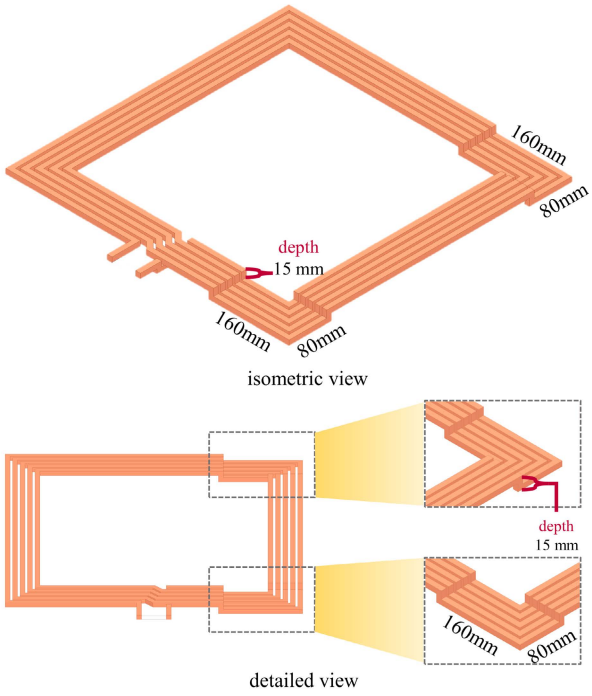

FIGURE 12. Proposed modular coil.

Furthermore, fluctuations in the received power may occur because of its non-flat property. Assume that the RX coil traverses the BP arrangement in Fig. 10. Because of the height difference in the two TX coils, the quantity of magnetic flux transferred from the two TX coils to the RX coil differs, causing fluctuations in the received power [34]. As a result, it may not be suited for DWPT environments where reliable power transfer is required when the RX is moving.

b: PROPOSED MODULAR COIL ARRAY

To solve the non-flat problem of the BP arrangement, the author of [34] provides a simple solution that bends one coil to share the same plane when configuring the BP arrangement. The solution, however, is confined to only two coils. To make an array for MIMO-WPT consisting of multiple coils, we propose an easily scalable coil shape based on a bending solution.

Fig. 12 shows the proposed modular coil based on the square coil in Fig. 9(a). The design principle of the proposed coil is lowering the depth of the partial overlap area at the flux cancellation point identified in Fig. 11. For this reason, in constructing an array, the proposed coil inherits the advantage of reducing cross-coupling of the BP arrangement, and it has a considerable advantage in terms of simple scalability. Fig. 13 shows an array configured as two proposed modular coils. By utilizing the proposed coils, configuring and expanding the array for MIMO-WPT is as simple as assembling a manufactured module; therefore, we refer to the proposed coil as a modular coil, and the array is a modular coil array.

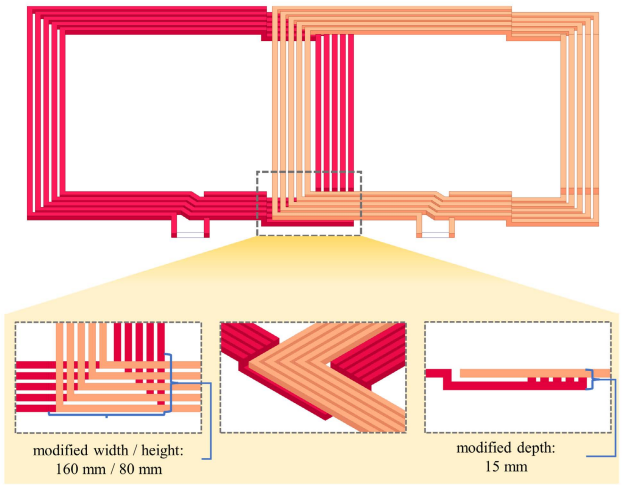

FIGURE 13. Array configured as two modular coils.

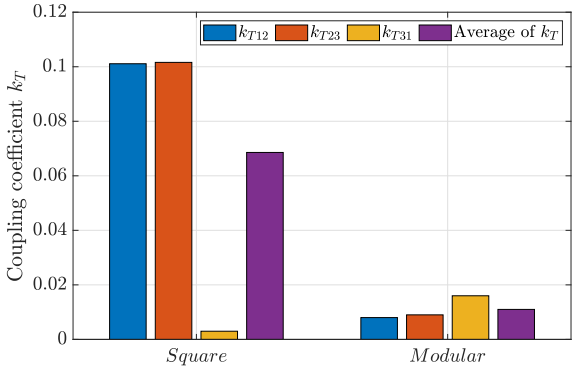

FIGURE 14. Coupling coefficient k_T of *Square* and *Modular*.

The detailed specifications of the modular coil are as follows. As shown in Fig. 11, the overlap width and height at the flux cancellation point are 150 mm and 70 mm, respectively. We modified the width and height to 160 mm and 80 mm, as shown in Fig. 13, to set a design and implementation margin. The depth of the modified area is 15 mm with a 5 mm margin.

2) COMPARISON BETWEEN SQUARE AND MODULAR COIL ARRAYS

As explained in Section III, the criteria of a magnetic coupler for MIMO-WPT with magnetic beamforming in terms of improved PTE and PF are as follows: 1) increased $\mathbf{M}$ between TX and RX arrays and 2) reduced $\mathbf{M_T}$ and $\mathbf{M_R}$ at TX and RX arrays. In this subsection, we compare the two arrays of the proposed modular coils (Fig. 13) and the existing array configured as square coils (Fig. 9(b)) to evaluate which array is most suitable for magnetic beamforming. We set each array to consist of three coils for a simpler comparison. The term *Square* stands for the existing square coil array, whereas the term *Modular* stands for the proposed modular coil array.

Fig. 14 shows a coupling coefficient k_T indicating the cross-coupling strength of the two arrays, and Fig. 15 shows a magnetic field plot when only TX 2 is excited. As shown in Fig. 14, the *Modular* successfully mitigates k_{T12} and k_{T23}

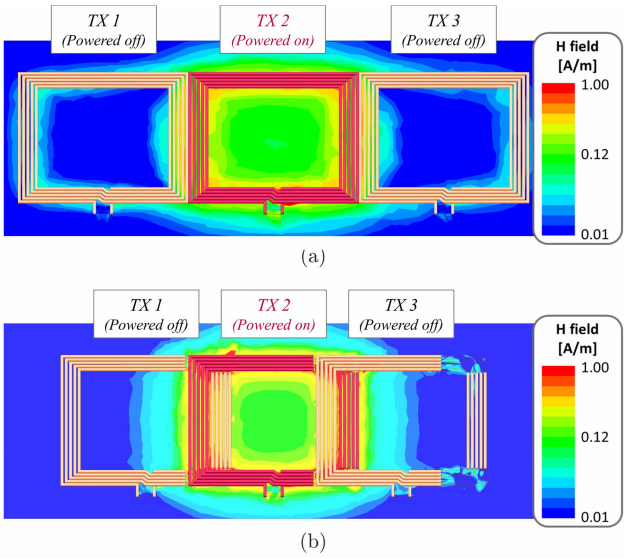

FIGURE 15. Magnetic field plot for analyzing the cross-couplings in array: (a) *Square* and (b) *Modular*.

between adjacent coils owing to the flux cancellation compared to *Square*. However, k_{T31} increases in the *Modular* compared to the *Square* due to the narrowed distance between TX 1 and 3, as shown in Fig. 15(b). Despite the *Modular*'s k_{T31} being higher than that of the *Square*, the *Square* has an average k_T of 0.07, whereas the *Modular* has an average k_T of approximately 0.01, which is significantly lower, as shown in the purple histogram in Fig. 14. This result can be verified through the magnetic field plot in Fig. 15. In the *Square* plot in Fig. 15(a), the voltage is induced at the adjacent TX 1 and TX 3 due to the cross-coupling, whereas little voltage is induced at the adjacent coils in the *Modular* plot in Fig. 15(b).

Additionally, the *Modular* provides a stronger magnetic coupling between the TX and RX array. As previously stated, the location where the RX coil is subjected to the weakest magnetic field is at the midpoint between two adjacent TX coils; thereby, the power pulsation phenomenon occurs at that location. The proposed *Modular* could offer a breakthrough to solve the power pulsation problem. Fig. 16 shows a magnetic field plot when a single RX coil is located at the midpoint of energized coil 1 and 2, and its height is 200 mm. As shown, more magnetic flux passes through the RX coil in the *Modular* than the *Square*. This is because the distance between TX coils 1 and 2 and the RX coil is narrowed due to overlapping structure in the *Modular*. The distance between the TX coils and the RX coil is about 300 mm and 360 mm, in the *Modular* and *Square*, respectively. For this reason, the amount of magnetic flux induced from each TX coil passing the RX coil increases. Fig. 17 shows an average coupling coefficient between the TX coils 1, 2, and the RX coil depending on the RX height at the midpoint of two TX coils. The result shows that the proposed *Modular* has a stronger magnetic coupling than the *Square* as the RX height varies.

Based on the above analyses, we have verified that the proposed modular coil array satisfies the criteria for improving

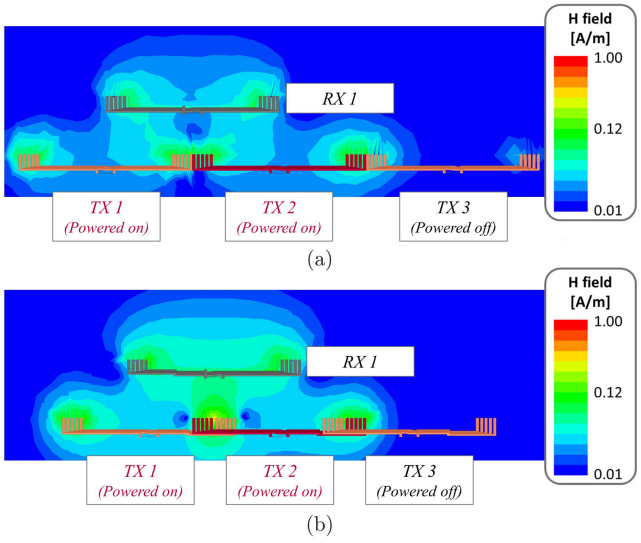

FIGURE 16. Magnetic field plot for analyzing magnetic couplings between TX and RX: (a) *Square* and (b) *Modular*.

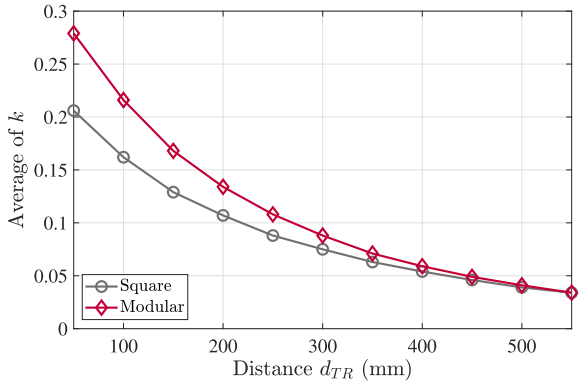

FIGURE 17. Coupling coefficient k depending on the charging distance.

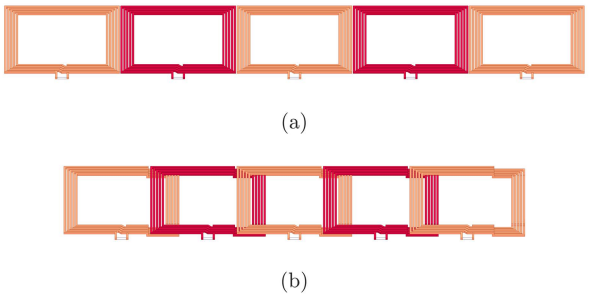

FIGURE 18. TX array configurations for simulation: (a) *Square* and (b) *Modular*.

the PTE and PF of a MIMO-WPT applying magnetic beamforming. For Section V, we configured the MIMO-WPT with the proposed modular coil in a DWPT environment to verify the improved performance via 3D FEM simulation.

V. PERFORMANCE COMPARISON IN A DWPT ENVIRONMENT

A. CONFIGURATIONS

Fig. 18 shows the candidates of the TX array configured as five coils for comparison. Fig. 19 shows TX and RX array deployment for simulation. As shown, the TX array

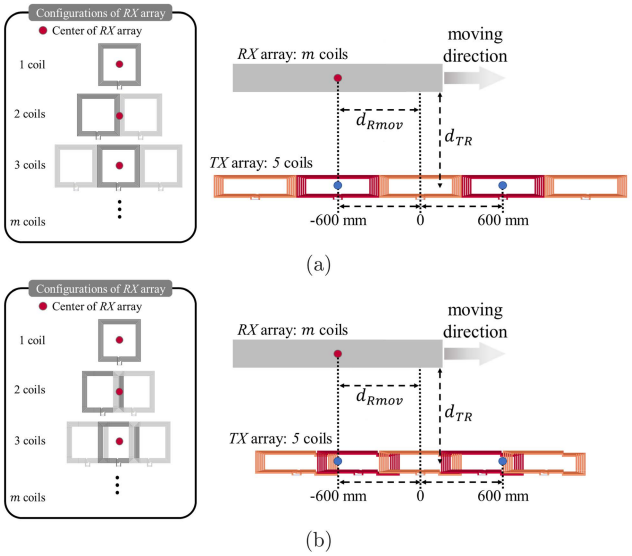

FIGURE 19. Array deployment for simulation: (a) *Square* and (b) *Modular*.

is fixed with five coil arrangements, whereas the RX array is configured as one to five coils. This adjustment shows the variation in performance relative to the area of the RX array. The height of the RX array, denoted by d_{TR}, was adjusted in 50 mm increments from 50 to 400 mm. To model a DWPT environment that charges a moving RX, the center of the RX array moves from -600 to 600 mm relative to the center of the TX array, as shown in Fig. 19. The term d_{Rmov} denotes the distance between the centers of the TX and RX arrays. The resonant frequency is set to 85 kHz, which is the industry standard for charging electric vehicles. Simulation parameters are included in Table 5.

B. MISO-WPT WITH MULTIPLE TX AND SINGLE RX

We carry out simulations of MISO-WPT having five TX coils and one RX coil (*i.e.*, 5×1 MISO-WPT). Fig. 20 shows the mutual inductance $\mathbf{M}$ when d_{TR} is 100 mm, as the distance d_{Rmov} is adjusted from -600 to +600 mm with respect to the center of TX array. Utilizing $\mathbf{M}$ in Fig. 20, the power transfer capability of the *Square* and *Modular* can be verified.

Comparing Fig. 20(a) and (b), the peak-to-peak distance is shorter for the *Modular* than for the *Square*. The *Modular* has a peak-to-peak distance of 450 mm due to the overlap for flux cancellation, while the *Square* has a peak-to-peak distance of about 600 mm, which is the width of one square coil. The TX array placed beneath each graph confirms this. As a result, the *Modular* has $\mathbf{M}$ of about 5.5 μH at the midpoint of two adjacent TX coils, which is greater than the *Square*'s $\mathbf{M}$ of around 4 μH. Next, the peak value of $\mathbf{M}$ of the *Square* is about 10 μH, while that of the *Modular* is slightly reduced below 10 μH. This is because the flux cancellation by the BP arrangement reduces the magnetic field delivered to the RX coil when the RX coil is situated in the center of each TX coil, thereby lowering the magnetic coupling strength.

TABLE 5. Parameters for simulations.

Parameter	Value	Description
Resonant frequency f_r	85 kHz	
Intrinsic resistance R_T, R_R	0.2 Ω	Derived
Load impedance R_L	5 Ω	
Total input power P_{in}	100 W	
Self inductance L_T, L_R	25 μH	Derived
Resonant capacitance C_T, C_R	5 nF	
Mutual inductance $\mathbf{M}$	Derived	
Mutual inductance $\mathbf{M_T}$, $\mathbf{M_R}$	Derived	
Compensation topology	Series-Series	

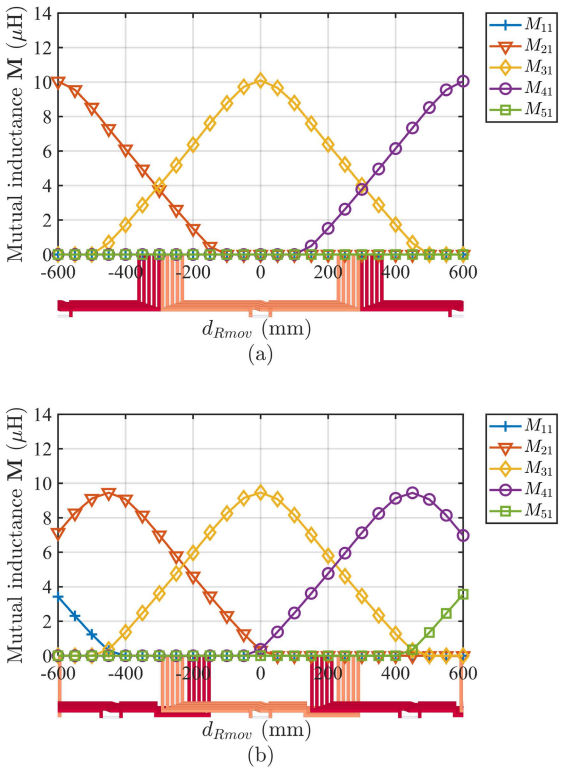

FIGURE 20. Mutual inductance *M* of MISO-WPT at d_{TR} = 100 mm: (a) *Square* and (b) *Modular*.

According to [21], the power transfer capability of WPT can be measured as the sum of the mutual inductance $\mathbf{M}$ denoted by $\sum \mathbf{M}$. Fig. 21 shows the sum of mutual inductance $\sum \mathbf{M}$ between the five TX coils and the single RX coil at d_{TR} from 100 to 400 mm when d_{Rmov} is adjusted from -600 to 600 mm. At d_{TR} of 100 mm, the average of the *Modular*'s $\sum \mathbf{M}$ is 10.5 μH with a deviation of 0.16 μH, whereas the average of the *Square*'s $\sum \mathbf{M}$ is 8.5 μH with a deviation of 0.86 μH. Other results show a similar tendency: the *Modular* has a higher average and lower deviation compared to the *Square*. Therefore, the *Modular* is expected to transfer more

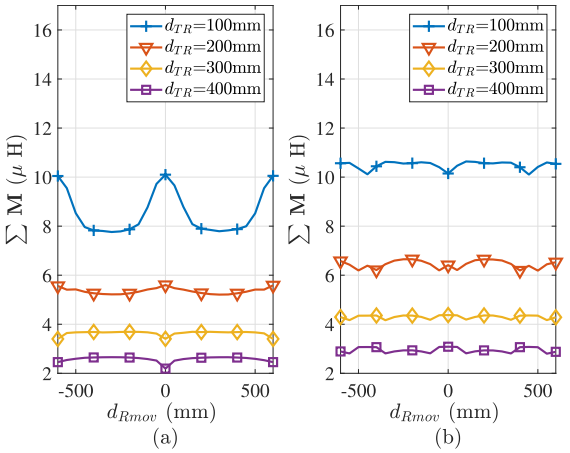

FIGURE 21. Sum of mutual inductance *M*: (a) *Square* and (b) *Modular*.

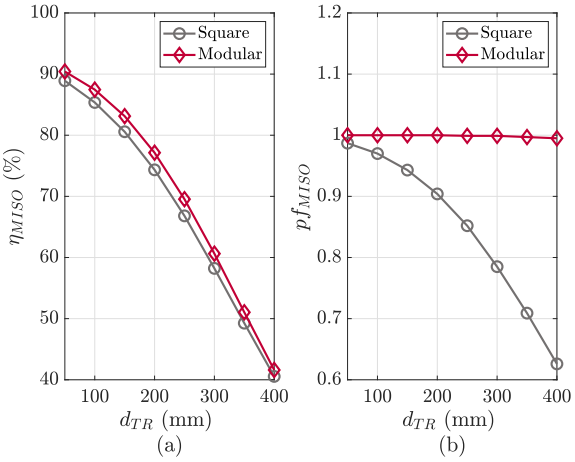

FIGURE 22. The results of 5 × 1 MISO-WPT: an average of (a) η_{MISO} and (b) pf_{MISO}.

power wirelessly with a lower deviation than the *Square* under the same input power.

From now on, the results provided are of a 5 × 1 MISO-WPT applying magnetic beamforming with $\mathbf{M}$ in Fig. 20. Fig. 22 shows the average results at d_{TR} from 50 to 400 mm: (a) η_{MISO} and (b) pf_{MISO}. The results in Fig. 20 are the average of the instantaneous outcomes when the RX coil traverses from -600 to 600 mm. Owing to the increased $\sum \mathbf{M}$ in Fig. 21, the *Modular* achieves a 1-2 % improvement in PTE η_{MISO} compared to the *Square*. Furthermore, the *Modular* keeps the average pf_{MISO} near 1.0 regardless of the d_{TR}, whereas that of the *Square* rapidly decreases as d_{TR} increases. The steep attenuation of pf_{MISO} in the *Square* is caused by the fact that the real part of the TX input impedance decreases as d_{TR} increases, whereas the imaginary part remains constant regardless of d_{TR}. On the other hand, the pf_{MISO} improvement of the *Modular* is attributable to the reduced cross-couplings at the TX coils, as shown in Fig. 14.

Fig. 23 shows an instantaneous η_{MISO} when the RX coil traverses from -600 to 600 mm relative to the center of the TX array. As shown in Fig. 23(a), the *Square* has the maximum η_{MISO} when the RX coil is at the center of the TX coil,

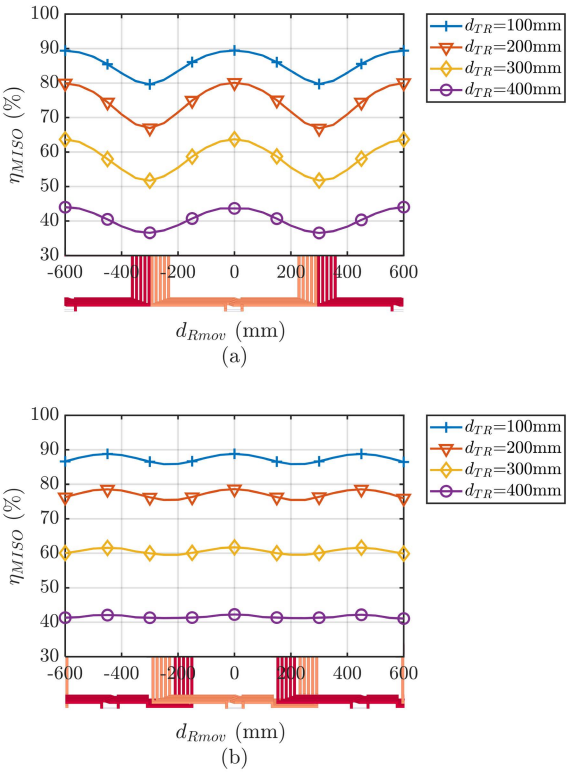

FIGURE 23. Instantaneous PTE η_{MISO}: (a) *Square* and (b) *Modular*.

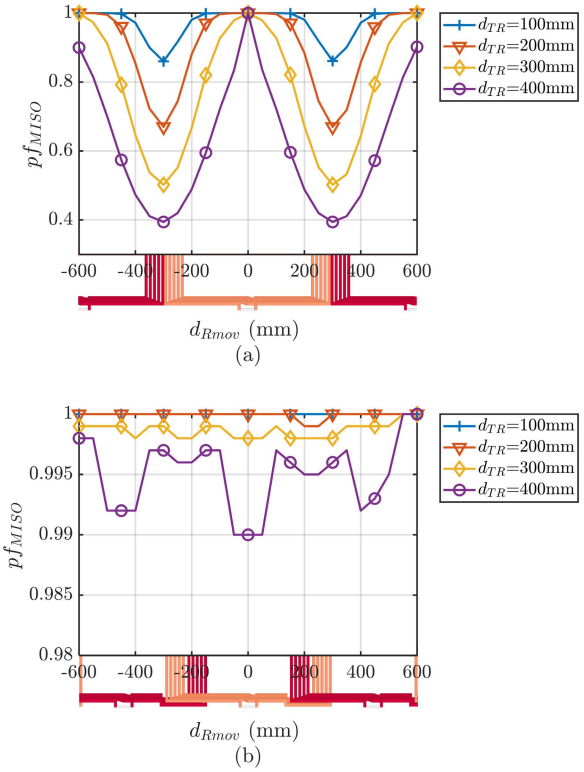

FIGURE 24. Instantaneous PF pf_{MISO}: (a) *Square* and (b) *Modular*.

while the minimum η_{MISO} is obtained when the RX coil is at the midpoint of two adjacent TX coils. This phenomenon is the power pulsation problem, as mentioned above. As the distance d_{TR} is adjusted from 100 to 400 mm, the maximum and minimum η_{MISO} differences are about 10, 13, 12, and 8 %, respectively. On the other hand, it is intuitively obvious that the *Modular* has less deviation of η_{MISO}, as shown in Fig. 23(b). In the *Modular*, for d_{TR} from 100 to 400 mm, the maximum and minimum η_{MISO} differences are approximately 3, 3, 2, and 1 %, respectively. This improvement is due to the *Modular* $\sum \mathbf{M}$ in Fig. 21 having small fluctuation. The results indicate that the *Modular* helps solve the power pulsation phenomenon encountered while the RX moves.

Fig. 24 shows an instantaneous pf_{MISO} under the same conditions. Similar to η_{MISO} in Fig. 23, the *Square* has the minimum pf_{MISO} when the RX coil is located between two adjacent TX coils and the maximum pf_{MISO} when the RX coil is at the center of the TX coil, as shown in Fig. 24(a). This result indicates that the RX coil is strongly affected by the cross-couplings of the TX array when it is located at the midpoint of two adjacent TX coils. Furthermore, as the distance d_{TR} increases from 100 to 400 mm, variation between the maximum and minimum pf_{MISO} value rapidly increases. This is because the reflected inductance by $\mathbf{M_T}$ is independent of d_{TR}, whereas the reflected resistance by $\mathbf{M}$ is inversely proportional to d_{TR}. Meanwhile, as shown in Fig. 24(b), the *Modular* maintains a pf_{MISO} close to 1.0 regardless of d_{TR}, owing to the reduction of $\mathbf{M_T}$.

Consequently, it is confirmed that the *Modular* achieves a more improved η_{MISO} and pf_{MISO} than the *Square* does due to the increased $\sum \mathbf{M}$ and reduced $\mathbf{M_T}$. Based on these results, the following subsection verifies the extent of performance improvement in MIMO-WPT provided by an increased number of RX coils.

C. MIMO-WPT WITH MULTIPLE TX AND RX COILS

In this subsection, we compared the performance of the *Square* and *Modular* applied for the MIMO-WPT. The MIMO-WPT configuration was as follows: five TX coils were deployed, and the number of RX coils was increased from two to five. This configuration allowed us to investigate changes in performance relative to the number and area of the RX arrays as the number of coils was increased. Fig. 25 shows the sum of mutual inductance $\mathbf{M}$ of two RX coils (RX 1 and 2) in the 5 × 2 MIMO-WPT. The $\sum \mathbf{M}$ in Fig. 25 has a nearly identical shape to $\sum \mathbf{M}$ of the MISO-WPT in Fig. 21, but the amplitude is twice as large. This is because each RX coil experiences the same mutual inductance in Fig. 10 while moving.

Fig. 26 shows the average results of η_{MIMO} of a 5 × 2 MIMO-WPT applying magnetic beamforming at d_{TR} from 50 to 400 mm. As can be seen, the *Modular* has about 4 % PTE improvement compared to the *Square*, which is superior to a 2 % PTE improvement of the SISO-WPT in Fig. 22(a). As shown in Fig. 22(a), the benefit of the proposed *Modular* in the MISO-WPT is not great at the long

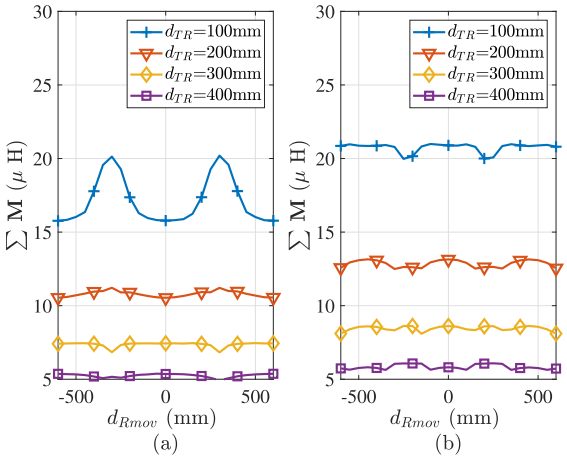

FIGURE 25. Sum of mutual inductance *M*: (a) *Square* and (b) *Modular*.

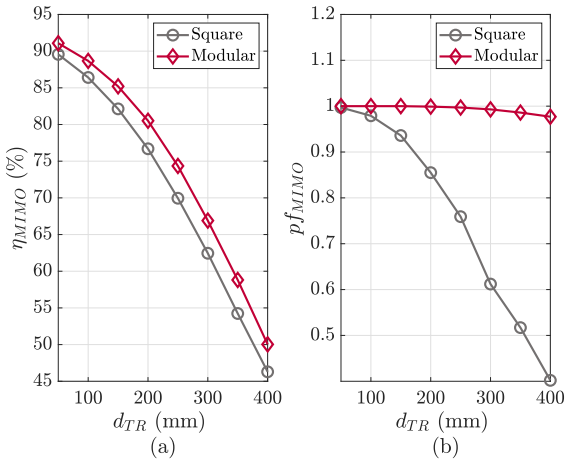

FIGURE 26. The results of 5 × 2 MIMO-WPT: an average of (a) PTE η_{MIMO} and (b) pf_{MIMO}.

d_{TR} because the PTE only depends on **M**. However, in the MIMO-WPT, the proposed *Modular* can provide at least a 4 % improvement in PTE far away from the TX array because it eliminates the large attenuation caused by RX cross-couplings. In other words, the *Modular*'s η_{MISO} improvement is only due to the increased **M**, whereas η_{MIMO} improvement is due to both increased **M** and lowered $\mathbf{M_R}$, resulting in a more notable improvement. Meanwhile, pf_{MIMO} in Fig. 26(b) exhibits the same tendency as pf_{MISO} in Fig. 22(b): pf_{MIMO} of the *Square* rapidly drops as d_{TR} increases, while that of the *Modular* is close to 1.0 regardless of d_{TR}. In this case, pf_{MIMO} has a higher attenuation rate than pf_{MISO} does. The cause of this phenomenon is explained in the following instantaneous results.

Fig. 27 shows an instantaneous η_{MIMO} when the RX array with two coils traverses from -600 to 600 mm relative to the center of the TX array. Similar to η_{MISO} in Fig. 23, the η_{MIMO} of the *Square* is on average lower and the deviation is larger than the η_{MIMO} of the *Modular*. The maximum and minimum η_{MIMO} differences in *Square* are about 5, 6, 4, and 3 %,

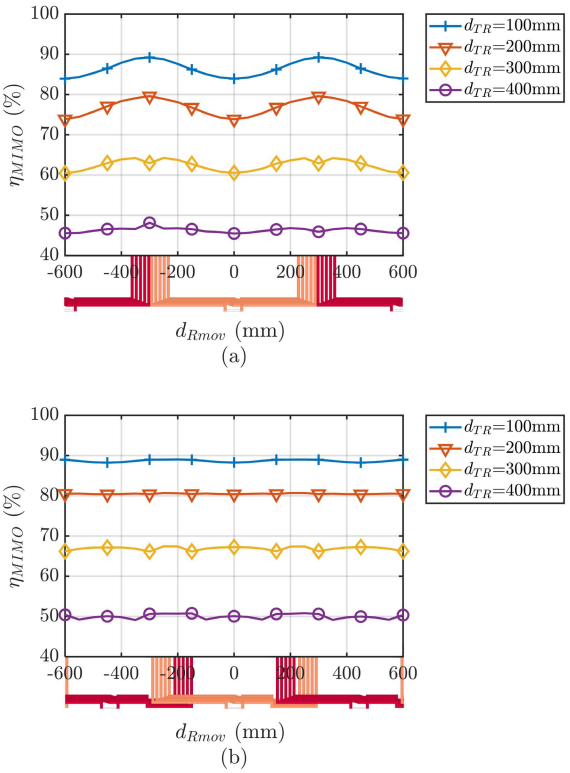

FIGURE 27. Instantaneous PTE η_{MISO}: (a) *Square* and (b) *Modular*.

respectively, for the d_{TR} from 100 to 400 mm. On the other hand, *Modular* has η_{MIMO} differences of roughly 1, 0.5, 1, and 2 %, respectively, at the same d_{TR}.

Fig. 28 shows an instantaneous pf_{MIMO} under the same conditions. The pf_{MIMO} of the *Square* rises and falls while the RX array is moving, which is the same tendency as with pf_{MISO} in Fig. 24(a). The *Square* has the maximum pf_{MIMO} when d_{Rmov} is 300 and -300 mm. This is because the two TX and RX coils are facing each other at these positions, resulting in the greatest reflected resistance. The minimum pf_{MIMO} is obtained when the RX array is located at the center of the TX array (*i.e.*, $d_{Rmov} = 0$). This indicates that the cross-couplings of TX 2 and 3, and TX 3 and 4 (*i.e.*, k_{T23} and k_{T34}) have more significant influence on pf_{MIMO} at this position. On the other hand, the *Modular* achieves higher pf_{MIMO} (0.97 or above), even when d_{TR} is 400 mm, which is slightly lower than the pf_{MISO} in Fig. 24. This is because, as the area of the RX array increases, more cross-coupling of the TX array affects the MIMO-WPT while transmitting power.

According to the results above, the *Modular* outperforms the *Square* in PTE and PF when used for MIMO-WPT. We repeated the same simulation with more RX coils to make the results more generic. The results of instantaneous η_{MIMO} and pf_{MIMO} according to the d_{Rmov} movement (Fig. 23, 24, 27, and 28) show similar tendencies regardless of the number of RX coils. Therefore, the instantaneous value according to the d_{Rmov} is omitted, whereas the average value is used as an indicator of performance.

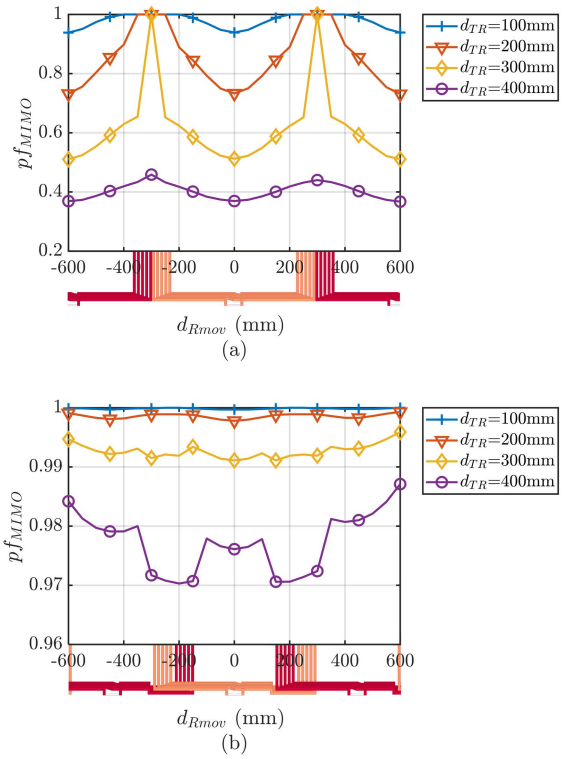

FIGURE 28. Instantaneous PF pf_{MISO}: (a) *Square* and (b) *Modular*.

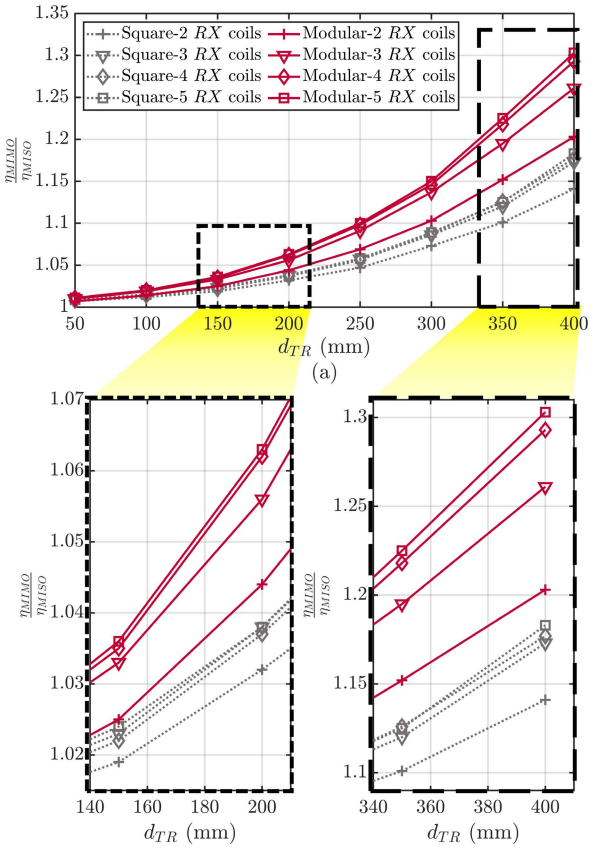

FIGURE 29. PTE variation depending on the number of RX coils.

Fig. 29 and Fig. 30 show the variation ratio of PTE and PF of the MIMO-WPT relative to those of the MISO-WPT (Fig. 29: η_{MIMO}/η_{MISO} and Fig. 30: pf_{MIMO}/pf_{MISO}), as the number of RX coils was adjusted from two to five. Both results confirm the influence of adjusting the number of RX coils on the WPT performance when the number of coils in the TX array is fixed.

Based on the graphs, two properties are confirmed in Fig. 29. First, both the *Square* and *Modular* show that the PTE improvement ratio, according to the increase in the number of RX coils, is more pronounced as the RX height d_{TR} increases. The highest PTE improvement ratios of the *Square* and *Modular* at 200 mm of d_{TR} are 3.8 % and 6.2 %, respectively. On the other hand, both arrays improve PTE up to 17 % and 30 % at 400 mm of d_{TR}, respectively, compared to that of the MISO-WPT. In other words, it is effective to configure the RX array with multiple coils for improving PTE when the RX height d_{TR} is farther. Second, the *Modular* has a higher overall PTE improvement ratio than the *Square*. As shown in Fig. 29, the *Modular* consistently outperforms the *Square* for the same number of RX coils. Even the *Modular* with two RX coils has a more remarkable PTE improvement than the *Square* with five RX coils. This intuitively indicates that using the *Modular* can improve PTE compared to the *Square*, even when the RX array area is small. As shown in Fig. 29, the *Square* has little PTE increases when the number of RX coils increases from two to five. As stated, this is because the cross-couplings at the several RX coils lower the magnetic coupling strength between the TX and RX coils, thereby reducing the amount of power transferred from the TX array.

On the other hand, the PF of MIMO-WPT drops as the number of RX coils increases in both the *Square* and *Modular*, as shown in Fig. 30. This phenomenon is more evident as the RX height d_{TR} increases. To express this intuitively, the PF is severely reduced if the area of the RX array is expanded to boost PTE at a long charging distance. There are two reasons for this phenomenon. First, the reflected resistance induced by the RX coils in the TX equivalent circuit decreases as the RX height d_{TR} increases, resulting in PF attenuation. Second, as the area of the RX array expands, more cross-couplings at the TX coils affect the WPT, which reduces the PF.

In the *Square*, the PF of MIMO-WPT is higher than that of the MISO-WPT when d_{TR} is less than 100 mm, as shown in the top-left graph in Fig. 30. This is because the reflected reactance caused by cross-coupling $\mathbf{M_R}$ at the RX array cancels out with the reflected inductance caused by cross-coupling $\mathbf{M_T}$ at the TX array, thus reducing the total reactance of the input impedance. However, because the reflection capacitance is inversely proportional to d_{TR}, it gradually decreases as d_{TR} increases; therefore, the reflected capacitance has almost no influence on the PF as d_{TR} increases. In addition, the *Modular* is robust compared to the *Square* in terms of PF variation according to the number of RX coils. When d_{TR} is 400 m, the PF variation of the *Square* reaches 50 %, whereas that of the *Modular* is just 10 %,

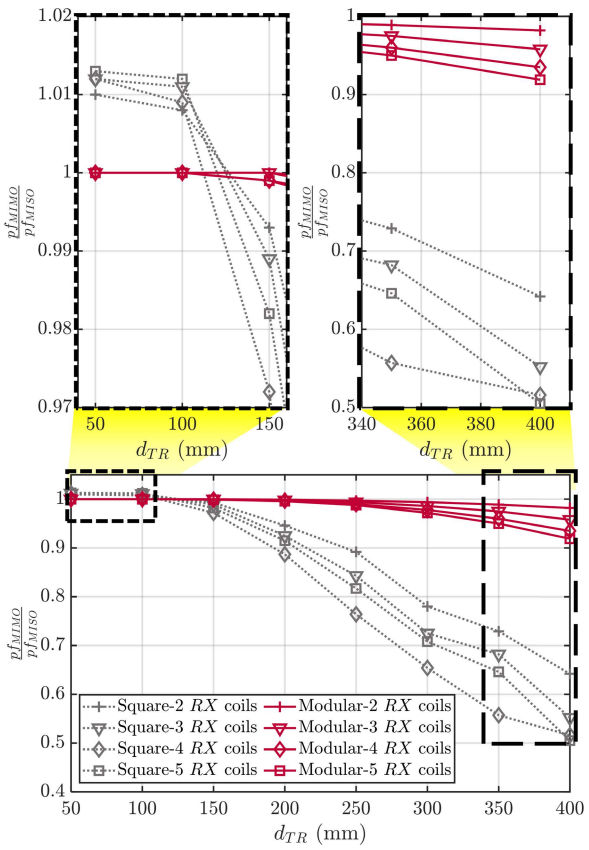

FIGURE 30. PF variation depending on the number of RX coils.

at most. This result is due to the advantages of the *Modular* that eliminates cross-couplings at the TX and RX coils and increases magnetic couplings between the TX and RX coils.

D. SUMMARY

When applied to the TX and RX arrays of MIMO-WPT, the suggested modular coil array outperforms the existing square coil array in terms of PTE and PF. While the RX array travels, the suggested modular coil array transfers constant power with minimum fluctuation, as opposed to the results with the existing square coil array. The PTE of the modular coil array improves as the number of RX coils rises, whereas the square coil array does not. Consequently, the suggested modular coil array has been shown to be suitable for use in a DWPT environment employing magnetic beamforming.

VI. CONCLUSION

In this paper, we first provided a theoretical analysis of magnetic couplings in MIMO-WPT (magnetic coupling between the TX and RX arrays, and cross-coupling at each TX and RX array) when applying magnetic beamforming. Our analysis showed the magnetic coupling criteria for improved PTE and PF performance: an increase in magnetic coupling between TX and RX arrays and a reduction of cross-coupling at TX and RX array. We also confirmed the validity of this criterion with a large number of coils using numerical analysis in MATLAB. Then, we proposed a modular coil array that can be used for MIMO-WPT. The proposed modular coil array can reduce cross-couplings at the TX and RX arrays and increase magnetic coupling between TX and RX array, satisfying the derived criteria for improved PTE and PF. There is also the benefit of having a flat surface and robust scalability when the proposed modular coils are arranged in an array. A 3D FEM simulation showed that the proposed modular coil array outperforms the existing square coil array in the DWPT environment.

Based on these findings, the proposed modular coil array is expected to be useful in various industries that use static or dynamic WPT. The proposed modular coil design can be optimized to achieve maximum performance in various applications by changing the geometry of the coil. For maximizing the PTE of the overall WPT system, such optimization must be combined with impedance matching, including load impedance optimization. Due to eliminating the cross-coupling, future work will allow receiver localization and weight calculation for magnetic beamforming to be realized with less computational complexity than in the traditional channel estimation method.

APPENDIX A
DERIVATION OF (10) AND (11)

- Magnetic channel $\mathbf{H}$ of (10)

In the SISO-WPT, the RX voltage is given by multiplying the $j\omega M$ by the TX current, as explained in (1). Thus, in the MIMO-WPT, the RX voltage $\overrightarrow{\mathbf{V_R}}$ is given by

$$\overrightarrow{\mathbf{V_R}} = j\omega\mathbf{M}\overrightarrow{\mathbf{I_T}}. \tag{30}$$

Since $\overrightarrow{\mathbf{V_R}}$ is calculated by $\overrightarrow{\mathbf{V_R}} = \mathbf{Z_R}\overrightarrow{\mathbf{I_R}}$, multiplying both sides of (30) by the inverse matrix of $\mathbf{Z_R}$ gives $\overrightarrow{\mathbf{I_R}} = j\omega\mathbf{Z_R^{-1}}\mathbf{M}\overrightarrow{\mathbf{I_T}}$. Here, the $j\omega\mathbf{Z_R^{-1}}\mathbf{M}$ term that directly relates $\overrightarrow{\mathbf{I_T}}$ and $\overrightarrow{\mathbf{I_R}}$ is defined as a magnetic channel $\mathbf{H}$ (*i.e.*, $\mathbf{H} = j\omega\mathbf{Z_R^{-1}}\mathbf{M}$).

- Matrix of reflected impedance $\mathbf{Z_T^R}$ of (11)

As above, in the MIMO-WPT, $\overrightarrow{\mathbf{V_T}}$ is given by

$$\overrightarrow{\mathbf{V_T}} = \mathbf{Z_T}\overrightarrow{\mathbf{I_T}} - j\omega\mathbf{M^T}\overrightarrow{\mathbf{I_R}}. \tag{31}$$

Substituting $\overrightarrow{\mathbf{I_R}} = j\omega\mathbf{Z_R^{-1}}\mathbf{M}\overrightarrow{\mathbf{I_T}}$ into (31) gives

$$\overrightarrow{\mathbf{V_T}} = \mathbf{Z_T}\overrightarrow{\mathbf{I_T}} + \omega^2\mathbf{M^T}\mathbf{Z_R^{-1}}\mathbf{M}\overrightarrow{\mathbf{I_T}}. \tag{32}$$

Here, the second term $\omega^2\mathbf{M^T}\mathbf{Z_R^{-1}}\mathbf{M}$ on the right side related to the $\overrightarrow{\mathbf{I_R}}$ is defined as a matrix of reflected impedance $\mathbf{Z_T^R}$ (*i.e.*, $\mathbf{Z_T^R} = \omega^2\mathbf{M^T}\mathbf{Z_R^{-1}}\mathbf{M}$).

APPENDIX B
SIMPLIFIED EQUATION OF BEAMFORMING CURRENT FOR SPECIFIC CONDITIONS
In N×2 MIMO-WPT

This Appendix B provides a simple equation of beamforming current $\overrightarrow{\mathbf{I}_T^{bf}}$ derived for $N \times 2$ MIMO-WPT. As shown in (21), the beamforming current for a typical MIMO-WPT requires

to calculate $\mathbf{H}^*\mathbf{R_R}\mathbf{H}$. Substituting the magnetic channel $\mathbf{H}$ of (10) into $\mathbf{H}^*\mathbf{R_R}\mathbf{H}$, it is calculated by $\mathbf{M}^*\mathbf{Z_R^{-1}}^*\mathbf{R_R}\mathbf{Z_R^{-1}}\mathbf{M}$.

Here, when the MIMO-WPT is configured as n TX and two RX coils A and B, $\mathbf{Z_R^{-1}}^*\mathbf{R_R}\mathbf{Z_R^{-1}}$ is given by

$$\mathbf{Z_R^{-1}}^*\mathbf{R_R}\mathbf{Z_R^{-1}} = \frac{1}{det\ (\mathbf{Z_R})}\begin{bmatrix} R_{Rb} & 0 \\ 0 & R_{Ra} \end{bmatrix}, \tag{33}$$

where $det\ (Z_R)$ is $Z_R = \omega^2 M_{ab}^2 + R_{Ra}R_{Rb}$. When the two RX circuits have the same resistance values (*i.e.*, $R_{Ra} = R_{Rb} = R_R$), $\mathbf{Z_R^{-1}}^*\mathbf{R_R}\mathbf{Z_R^{-1}}$ becomes a constant by (33). Thus, $\mathbf{H}^*\mathbf{R_R}\mathbf{H}$ of (21) is abbreviated to $\mathbf{M}^T\mathbf{M}$, which results that the beamforming current $\overrightarrow{\mathbf{I}_T^{bf}}$ is given by $\overrightarrow{\mathbf{I}_T^{bf}} = c' \cdot maxeig\ (\mathbf{M}^*\mathbf{M})$.

REFERENCES

[1] D. Patil, M. K. McDonough, J. M. Miller, B. Fahimi, and P. T. Balsara, "Wireless power transfer for vehicular applications: Overview and challenges," *IEEE Trans. Transport. Electrific.*, vol. 4, no. 1, pp. 3–37, Mar. 2018.

[2] K. Aditya, V. K. Sood, and S. S. Williamson, "Magnetic characterization of unsymmetrical coil pairs using Archimedean spirals for wider misalignment tolerance in IPT systems," *IEEE Trans. Transport. Electrific.*, vol. 3, no. 2, pp. 454–463, Jun. 2017.

[3] H.-J. Kim, H. Hirayama, S. Kim, K. J. Han, R. Zhang, and J.-W. Choi, "Review of near-field wireless power and communication for biomedical applications," *IEEE Access*, vol. 5, pp. 21264–21285, 2017.

[4] C. Panchal, S. Stegen, and J. Lu, "Review of static and dynamic wireless electric vehicle charging system," *Eng. Sci. Technol., Int. J.*, vol. 21, no. 5, pp. 922–937, 2018.

[5] J. Xu, Y. Zeng, and R. Zhang, "UAV-enabled wireless power transfer: Trajectory design and energy optimization," *IEEE Trans. Wireless Commun.*, vol. 17, no. 8, pp. 5092–5106, Aug. 2018.

[6] J. Chen, J. Liu, Z. Sun, W. Chen, and L. Zhang, "Research on passive control strategy of AGV wireless power transfer system," in *Proc. 34rd Youth Academic Annu. Conf. Chin. Assoc. Automat. (YAC)*, Jun. 2019, pp. 200–205.

[7] P. K. S. Jayathurathnage, A. Alphones, D. M. Vilathgamuwa, and A. Ong, "Optimum transmitter current distribution for dynamic wireless power transfer with segmented array," *IEEE Trans. Microw. Theory Techn.*, vol. 66, no. 1, pp. 346–356, Jan. 2018.

[8] M. Budhia, G. A. Covic, and J. T. Boys, "Design and optimization of circular magnetic structures for lumped inductive power transfer systems," *IEEE Trans. Power Electron.*, vol. 26, no. 11, pp. 3096–3108, Nov. 2011.

[9] F. Lu, H. Zhang, H. Hofmann, and C. Mi, "A dynamic charging system with reduced output power pulsation for electric vehicles," *IEEE Trans. Ind. Electron.*, vol. 63, no. 10, pp. 6580–6590, Oct. 2016.

[10] J. P. K. Sampath, D. M. Vilathgamuwa, and A. Alphones, "Efficiency enhancement for dynamic wireless power transfer system with segmented transmitter array," *IEEE Trans. Transport. Electrific.*, vol. 2, no. 1, pp. 76–85, Mar. 2016.

[11] J. Jadidian and D. Katabi, "Magnetic mimo: How to charge your phone in your pocket," in *Proc. 20th Annu. Int. Conf. Mobile Comput. Netw.*, 2014, pp. 495–506.

[12] L. Shi, Z. Kabelac, D. Katabi, and D. Perreault, "Wireless power hotspot that charges all of your devices," in *Proc. 21st Annu. Int. Conf. Mobile Comput. Netw.*, Sep. 2015, pp. 2–13.

[13] B. H. Waters, B. J. Mahoney, V. Ranganathan, and J. R. Smith, "Power delivery and leakage field control using an adaptive phased array wireless power system," *IEEE Trans. Power Electron.*, vol. 30, no. 11, pp. 6298–6309, Nov. 2015.

[14] R. Johari, J. V. Krogmeier, and D. J. Love, "Analysis and practical considerations in implementing multiple transmitters for wireless power transfer via coupled magnetic resonance," *IEEE Trans. Ind. Electron.*, vol. 61, no. 4, pp. 1774–1783, Apr. 2013.

[15] K. Kim, H.-J. Kim, D.-W. Seo, and J.-W. Choi, "Analysis on influences of intra-couplings in a MISO magnetic beamforming wireless power transfer system," *Energies*, vol. 14, no. 16, p. 5184, Aug. 2021.

[16] Y. Wang, P. Gu, Y. Yao, and D. Xu, "Analysis and design of cubic magnetic coupler for high distance-to-diameter ratio IPT systems," *IEEE Trans. Ind. Electron.*, vol. 69, no. 1, pp. 409–419, Jan. 2022.

[17] S. Kisseleff, I. F. Akyildiz, and W. Gerstacker, "Beamforming for magnetic induction based wireless power transfer systems with multiple receivers," in *Proc. IEEE Global Commun. Conf. (GLOBECOM)*, Dec. 2015, pp. 1–7.

[18] S.-S. Yoo, K.-Y. Lee, and H.-J. Yoo, "Coupling-shielded inductor for high isolation between PA and *LC*-based DCO," *IEEE Electron Device Lett.*, vol. 38, no. 1, pp. 24–27, Nov. 2016.

[19] H.-J. Kim, J. Park, K.-S. Oh, J. P. Choi, J. E. Jang, and J. W. Choi, "Near-field magnetic induction MIMO communication using heterogeneous multipole loop antenna array for higher data rate transmission," *IEEE Trans. Antennas Propag.*, vol. 64, no. 5, pp. 1952–1962, May 2016.

[20] S. C. Tang, S. Y. Hui, and H. S.-H. Chung, "Evaluation of the shielding effects on printed-circuit-board transformers using ferrite plates and copper sheets," *IEEE Trans. Power Electron.*, vol. 17, no. 6, pp. 1080–1088, Nov. 2002.

[21] Y. Li, J. Hu, T. Lin, X. Li, F. Chen, Z. He, and R. Mai, "A new coil structure and its optimization design with constant output voltage and constant output current for electric vehicle dynamic wireless charging," *IEEE Trans. Ind. Informat.*, vol. 15, no. 9, pp. 5244–5256, Sep. 2019.

[22] J. Deng, W. Li, T. D. Nguyen, S. Li, and C. C. Mi, "Compact and efficient bipolar coupler for wireless power chargers: Design and analysis," *IEEE Trans. Power Electron.*, vol. 30, no. 11, pp. 6130–6140, Nov. 2015.

[23] S. Kim, G. A. Covic, and J. T. Boys, "Tripolar pad for inductive power transfer systems for EV charging," *IEEE Trans. Power Electron.*, vol. 32, no. 7, pp. 5045–5057, Jul. 2017.

[24] M. Fu, T. Zhang, P. C.-K. Luk, X. Zhu, and C. Ma, "Compensation of cross coupling in multiple-receiver wireless power transfer systems," *IEEE Trans. Ind. Informat.*, vol. 12, no. 2, pp. 474–482, Apr. 2016.

[25] A. Ahmad, M. S. Alam, and R. Chabaan, "A comprehensive review of wireless charging technologies for electric vehicles," *IEEE Trans. Transport. Electrific.*, vol. 4, no. 1, pp. 38–63, Mar. 2018.

[26] C. K. Alexander, M. N. Sadiku, and M. Sadiku, *Fundamentals of Electric Circuits*, vol. 4. New York, NY, USA: McGraw-Hill, 2009.

[27] J. D. Glover, M. S. Sarma, and T. Overbye, *Power System Analysis & Design, SI Version*. Boston, MA, USA: Cengage Learning, 2012.

[28] S. U. Pillai, T. Suel, and S. Cha, "The Perron–Frobenius theorem: Some of its applications," *IEEE Signal Process. Mag.*, vol. 22, no. 2, pp. 62–75, Mar. 2005.

[29] G. Strang, *Introduction to Linear Algebra*. Wellesley, MA, USA: Wellesley-Cambridge Press, 1993. vol. 3.

[30] R. Huang, B. Zhang, D. Qiu, and Y. Zhang, "Frequency splitting phenomena of magnetic resonant coupling wireless power transfer," *IEEE Trans. Magn.*, vol. 50, no. 11, pp. 1–4, Nov. 2014.

[31] Z. Duan, Y.-X. Guo, and D.-L. Kwong, "Rectangular coils optimization for wireless power transmission," *Radio Sci.*, vol. 47, no. 3, pp. 1–10, Jun. 2012.

[32] Z. Luo and X. Wei, "Analysis of square and circular planar spiral coils in wireless power transfer system for electric vehicles," *IEEE Trans. Ind. Electron.*, vol. 65, no. 1, pp. 331–341, Jan. 2018.

[33] G. A. Covic, M. L. G. Kissin, D. Kacprzak, N. Clausen, and H. Hao, "A bipolar primary pad topology for EV stationary charging and highway power by inductive coupling," in *Proc. IEEE Energy Convers. Congr. Exposit.*, Sep. 2011, pp. 1832–1838.

[34] A. Zaheer, G. A. Covic, and D. Kacprzak, "A bipolar pad in a 10-kHz 300-W distributed IPT system for AGV applications," *IEEE Trans. Ind. Electron.*, vol. 61, no. 7, pp. 3288–3301, Jul. 2014.

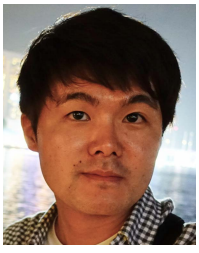

KYUNGTAE KIM received the B.S. degree in electronic engineering from Kyungpook National University (KNU), Daegu, South Korea, in 2013, and the M.S. degree in electrical engineering from the Daegu Gyeongbuk Institute of Science and Technology (DGIST), Daegu, in 2018, where he is currently pursuing the Ph.D. degree in electrical engineering. From 2013 to 2016, he worked as an Electrical Engineer with the High-Tech Division, Samsung C&T, Hwaseong-si, South Korea; and Bac Ninh, Vietnam. His research interests include magnetic beamforming, wireless power transfer, and cellular vehicle-to-everything communication.

HAN-JOON KIM (Member, IEEE) received the B.S. and M.S. degrees in information control and instrumentation engineering from Kwangwoon University, Seoul, South Korea, in 2011 and 2013, respectively, and the Ph.D. degree in information and communication engineering from the Daegu Gyeongbuk Institute of Science and Technology (DGIST), Daegu, South Korea, in 2018. He was a Postdoctoral Researcher with the Brain Engineering Convergence Research Center, DGIST, in 2018. Since 2019, he has been with a Research Fellow with the Electrical and Computer Engineering Department, National University of Singapore (NUS). His research interests include robotics, magnetic communication, wireless power transfer, and bio-medical applications using electromagnetics.

DONG-WOOK SEO (Senior Member, IEEE) received the B.S. degree in electrical engineering from Kyungpook National University, Daegu, South Korea, in 2003, and the M.S. and Ph.D. degrees in electrical engineering from the Korea Advanced Institute of Science and Technology (KAIST), Daejeon, South Korea, in 2005 and 2011, respectively. He was a Senior Researcher of the Defense Agency for Technology and Quality (DTaQ), Daegu, from 2011 to 2012. From 2012 to 2017, he was a Senior Researcher with the Electronics and Telecommunications Research Institute (ETRI), Daegu. Since September 2017, he has been with Korea Maritime and Ocean University (KMOU), Busan, South Korea, where he is currently an Associate Professor with the Division of Electronics and Electrical Information Engineering. His current research interests include numerical techniques in the areas of electromagnetics, radar cross-section analysis, wireless power transfer, and automotive radar systems.

JI-WOONG CHOI (Senior Member, IEEE) received the B.S., M.S., and Ph.D. degrees from Seoul National University, Seoul, South Korea, in 1998, 2000, and 2004, respectively, all in electrical engineering. From 2004 to 2005, he was a Postdoctoral Researcher with the Inter-University Semiconductor Research Center, SNU. From 2005 to 2007, he was a Postdoctoral Visiting Scholar with the Department of Electrical Engineering, Stanford University, Stanford, CA, USA. He was also a Consultant with GCT Semiconductor, San Jose, CA, USA, for development of mobile TV receivers, from 2006 to 2007. From 2007 to 2010, he was with Marvell Semiconductor, Santa Clara, CA, USA, as a Staff Systems Engineer for next-generation wireless communication systems, including WiMAX and LTE. Since 2010, he has been with the Department of Electrical Engineering and Computer Science, Daegu Gyeongbuk Institute of Science and Technology (DGIST), Daegu, South Korea, as a Professor. His research interests include wireless communication theory, signal processing, biomedical communication applications, and brain–machine interface.